

A deep-learning based generalized reduced-order model of glottal flow during normal phonation

Yang Zhang,¹ Weili Jiang,¹ Luning Sun,² Jianxun Wang,² Simeon Smith,³ Ingo R. Titze,³ Xudong Zheng,^{1, a} and Qian Xue^{1, b}

¹*Department of Mechanical Engineering, University of Maine, Orono, ME, 04469, USA*

²*Department of Aerospace and Mechanical Engineering, University of Notre Dame, Notre Dame, IN, 46556, USA*

³*The National Center for Voice and Speech, University of Utah, Salt Lake City, UT, 84101, USA*

(Dated: 26 May 2020)

1 This paper proposes a deep-learning based generalized reduced-order model (ROM)
2 that can provide a fast and accurate prediction of the glottal flow during normal
3 phonation. The approach is based on the assumption that the vibration of the vocal
4 folds can be represented by a universal kinematics equation (UKE), which is used
5 to generate a glottal shape library. For each shape in the library, the ground truth
6 values of the flow rate and pressure distribution are obtained from the high-fidelity
7 Navier-Stokes (N-S) solution. A fully-connected deep neural network (DNN) is then
8 trained to build the empirical mapping between the shapes and the flow rate and
9 pressure distributions. The obtained DNN based reduced-order flow solver is coupled
10 with a finite-element method (FEM) based solid dynamics solver for FSI simulation of
11 phonation. The reduced-order model is evaluated by comparing to the Navier-Stokes
12 solutions in both static glottal shapes and FSI simulations. The results demonstrate
13 a good prediction performance in accuracy and efficiency.

^axudong.zheng@maine.edu

^bqian.xue@maine.edu

14 I. INTRODUCTION

15 Voiced sound production in the human larynx is a complex fluid-structure interaction
16 (FSI) process in which the forced air from the lungs interacts with vocal fold tissues to initiate
17 sustained vibrations that modulate the glottal airflow (Titze, 1994). An accurate prediction
18 of the vocal fold vibration and sound source relies on an accurate prediction of intraglottal
19 pressure and glottal flow rate. In the past, the most commonly used glottal flow model for
20 simulating FSI is the Bernoulli equation which simplifies the flow as a 1D inviscid flow (Ruty
21 *et al.*, 2007; Wurzbacher *et al.*, 2006; Zanartu *et al.*, 2007). By coupling with lumped-mass
22 or continuum vocal fold models, the model has provided important understandings of the
23 dynamics of FSI during voice production (Alipour *et al.*, 2000; Erath *et al.*, 2011; Ishizaka
24 and Flanagan, 1972; Jiang and Zhang, 2002; Steinecke and Herzel, 1995; Story and Titze,
25 1995; Tao and Jiang, 2008; Titze, 1988; Zhang and Jiang, 2008). Yet, the inviscid assumption
26 has made the model inaccurate in predicting the glottal flow rate and intraglottal pressures,
27 especially during glottal closing when the glottis is typically in a divergent shape in which
28 rich viscous effects occur such as flow separation, shear layer instability and intraglottal
29 vortices (Deverge *et al.*, 2003; Pelorson *et al.*, 1994; Scherer *et al.*, 1983). To improve the
30 accuracy, research efforts have been made to incorporate various viscous loss terms into the
31 Bernoulli equation (Deverge *et al.*, 2003; Ishizaka and Flanagan, 1972; Van den Berg *et al.*,
32 1957; Zhang and Yang, 2016). While the results showed improvement over the original
33 Bernoulli equation, the modified model is largely based on assumptions of simple glottal
34 shapes. On the other hand, the quick advancement of the continuum vocal fold model from

35 simple 2D configurations to complex 3D subject-specific configurations increasingly requires
36 a more sophisticated glottal flow model that can represent glottal flow dynamics in complex
37 glottal shapes. The Navier-Stokes (N-S) equation based model, i.e., the full-order model
38 (FOM) can satisfy the requirement (Luo *et al.*, 2008; Mittal *et al.*, 2011; Xue *et al.*, 2014;
39 Zheng *et al.*, 2010), but the very high computational cost limits its use in statistical studies.
40 Therefore, there is a need and interest in developing a glottal flow model that can provide
41 accurate and fast solution of glottal flow dynamics in complex glottal shapes.

42 It has been shown that self-sustained oscillation of vocal folds is dominated by a few
43 modes of vibration, even when the motion is abnormal (Berry, 2001; Berry *et al.*, 1994;
44 Döllinger *et al.*, 2005). This high predictability of the vibratory pattern of the vocal folds
45 makes it feasible to model the glottal flow dynamics based on the glottal shapes using
46 deep-learning approach. Nevertheless, related research focusing on this area is still rare. A
47 deep-learning based reduced-order model (ROM) model for glottal flow was proposed in our
48 previous study (Zhang *et al.*, 2020). The model was based on the Bernoulli equation with
49 a viscous loss term predicted by a deep neural network (DNN) model. With the trained
50 DNN-Bernoulli model, the flow resistance coefficient as well as the flow rate and pressure
51 distribution of a given glottal shape can be predicted. However, the DNN-Bernoulli model
52 was developed under certain initial and geometry conditions and the generalization ability
53 of the model may be limited. In this paper, a deep-learning based generalized ROM of
54 the glottal flow during normal phonations is proposed. The underlying assumption of the
55 approach is that the vocal fold kinematics can be approximated by a few vibration modes
56 described by the surface-wave approach (Smith and Titze, 2018). A number of past studies

57 showed that the vocal fold vibration in normal phonation is dominated by two modes (Berry,
58 2001; Berry *et al.*, 1994; Döllinger *et al.*, 2005; Smith and Titze, 2018). Therefore, in the
59 present work, we assume that the vibration of the vocal folds is approximated by a linear
60 combination of the modal displacement of the two dominant modes, and then a universal
61 kinematics equation (UKE) can be obtained. The UKE is examined by generating a large
62 number of glottal shapes from FSI simulations with various vocal fold material properties and
63 subglottal pressures and fitting the glottal shapes with the UKE using the genetic algorithm
64 (GA) (Forrest, 1996; Goldberg, 2006; Mitchell, 1998). The probability distribution function
65 (PDF) of each fitting parameter is then obtained and used to construct a generalized glottal
66 shape library by appropriately resampling the PDF of the fitting parameters. For each shape
67 in the library, the ground truth value of the flow rate and pressure distribution are obtained
68 from high-fidelity N-S solutions. A fully-connected DNN (Goodfellow *et al.*, 2016) is then
69 used to build the empirical mapping between input parameters (fitting parameters in the
70 UKE and subglottal pressure) and output parameters (flow rate and pressure distribution).
71 K-fold cross validation is performed to fine tune the architecture and hyperparameters and
72 evaluate the prediction performance of the DNN. The developed reduced order glottal flow
73 model is therefore composed of two parts: (a) glottal shape parameterization using the UKE
74 and GA, and (b) glottal flow rate and intraglottal pressure prediction using the trained DNN.
75 The performance of the developed flow model (ROM) is evaluated by comparing to the N-S
76 solutions (FOM) in both static glottal shapes and FSI simulations.

77 The outline of the paper is organized as follows: the three-dimensional shape of the vocal
78 fold during vibration, including the prephonatory geometry and UKE, are introduced in

79 Section II; the process of building up the generalized glottal shape library is elaborated in
80 Section III; details about the implementation and evaluation of the DNN model are discussed
81 in Section IV; implementation and evaluation of the performance of the present ROM for
82 FSI Simulation are discussed in Section V; finally, the conclusions are summarized in Section
83 VI.

84 II. THREE-DIMENSIONAL SHAPE OF VOCAL FOLD DURING VIBRATION

85 A. Prephonatory Geometry

86 The prephonatory geometry of the vocal fold (right half) is shown in Figure 1. The
87 length L along the anterior-posterior direction (z), medial surface thickness T along the
88 inferior-superior direction (y) and depth D along the lateral direction (x) are $1.5cm$, $0.3cm$
89 and $0.75cm$, respectively. The subglottal angle α equals to $\arctan 0.5$. An initial gap $\Delta x =$
90 $0.002cm$ along the lateral direction (x) exists between the left and right counterpart. The
91 vocal fold is divided into three layers including the cover, ligament, and body. The thickness
92 of the cover (T_C) and ligament (T_L) layers are both $0.05cm$. Each layer is assumed to be
93 invariant in the anterior-posterior direction.

94 B. Universal Kinematics Equation (UKE)

95 Past studies have shown that vocal fold vibrations are dominated by a few vibratory
96 modes (Berry, 2001; Berry *et al.*, 1994; Döllinger *et al.*, 2005). Following the surface-wave
97 approach in (Titze, 1988), these modes can be described with a combination of (m,n) modes,

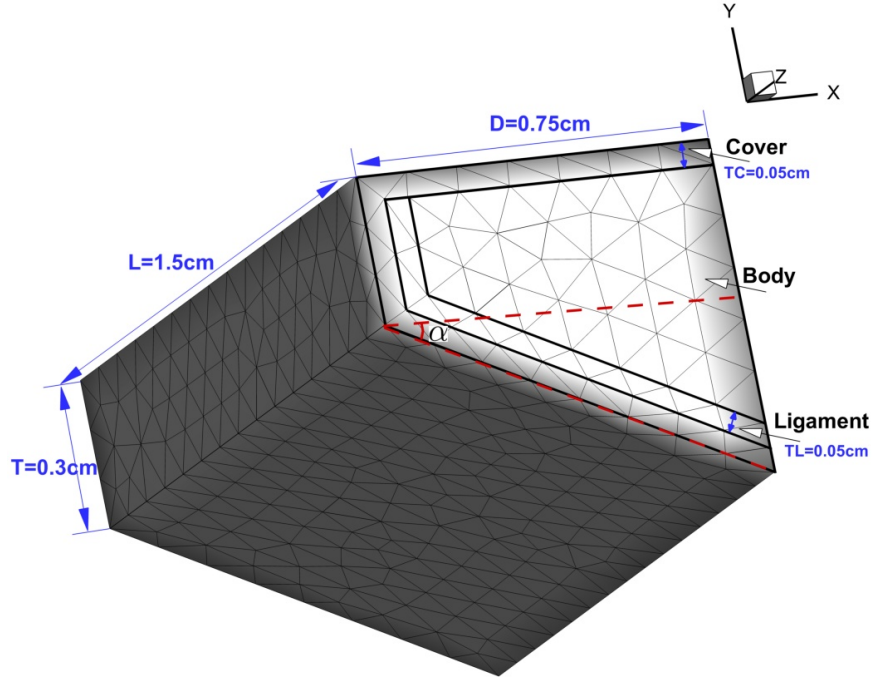


FIG. 1. Prephonatory geometry of the vocal fold.

98 where m and n correspond to the number of half-wavelengths in the anterior-posterior and
 99 inferior-superior directions, respectively. For normal phonation, the most dominant modes
 100 are the $(1, 0)$ and $(1, 1)$ modes, where $(1, 0)$ represents the in-phase vibration and $(1, 1)$
 101 represents the out-of-phase vibration (Smith and Titze, 2018; Titze, 1988). Taking the right-
 102 half vocal fold model in Figure 1 as an example, the displacement of the medial surface over
 103 time can be represented by a linear combination of the modal displacement of these two
 104 modes,

$$\xi(y, z, t) = \alpha \xi(y, z, t)_{(1,0)} + (1 - \alpha) \xi(y, z, t)_{(1,1)}, \quad (1)$$

105 where the subscripts (1, 0) and (1, 1) respectively refer to modes (1, 0) and (1, 1), and α is
 106 the weight coefficient of mode (1, 0). An equivalent equation exists for the left-half vocal
 107 fold. An example of the modal shape of the right-half vocal fold is illustrated in Figure 2,
 108 where the subfigures (a) and (b) respectively represent the modal shape (1, 0) and (1, 1) of
 109 the vocal fold, and the subfigures (c), (d) and (e) represent the actual shape of the vocal
 110 fold obtained from Eq. (1) with $\alpha = \frac{1}{4}$, $\frac{1}{2}$ and $\frac{3}{4}$, respectively. Note that in our study, to
 111 simplify the model, only the lateral (x) vibration is allowed and the vertical (y) motion is
 112 fixed.

113 In (Smith and Titze, 2018), based on the surface-wave approach and small-angle approx-
 114 imation (Titze, 1988), the modal displacement of the medial surface of the vocal fold at any
 115 instant in time were defined as,

$$\xi(y, z, t)_{(m,n)} = \xi_m \sin(m\pi z/L) [\sin \omega t - n(\omega/c)(y - y_m) \cos \omega t], \quad (2)$$

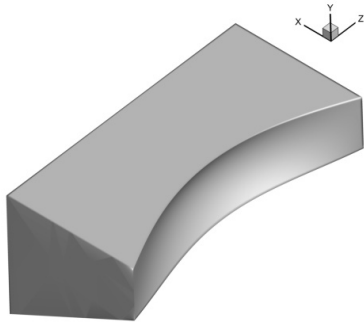
116 where ξ_m is the modal displacement amplitude, y_m is the inflection point for the vertical
 117 half wavelength, ω is angular frequency, and c is the speed of the mucosal wave.

118 The displacement of the medial surface of the vocal fold over time in Eq. (1) can then
 119 be expressed as,

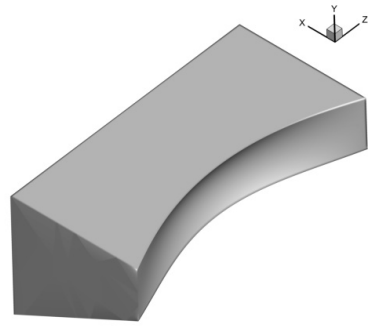
$$\xi(y, z, t) = \xi_m \sin(\pi z/L) [\sin \omega t - (1 - \alpha)(\omega/c)(y - y_m) \cos \omega t], \quad (3)$$

120 where y_m is the inflection point for the vertical half wavelength (Smith and Titze, 2018).
 121 Note that our later FSI simulation results reflected that the location of the inflection point
 122 changes along the anterior-posterior direction, therefore, the inflection location is modeled as

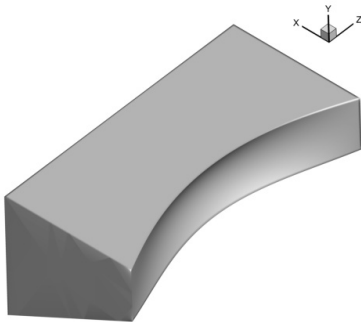
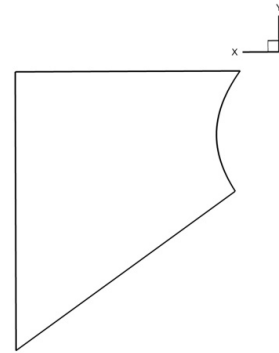
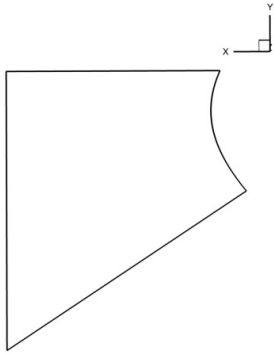
$$y_m = T - \beta \left(\sin \frac{\pi z}{L} + 1 \right), \quad (4)$$



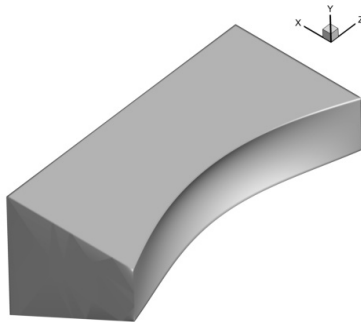
(a) Mode (1,0)



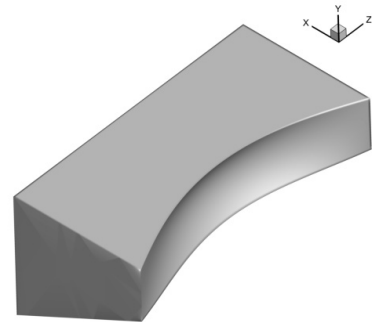
(b) Mode (1,1)



(c) $\frac{1}{4}$ Mode (1,0) + $\frac{3}{4}$ Mode (1,1)



(d) $\frac{1}{2}$ Mode (1,0) + $\frac{1}{2}$ Mode (1,1)



(e) $\frac{3}{4}$ Mode (1,0) + $\frac{1}{4}$ Mode (1,1)

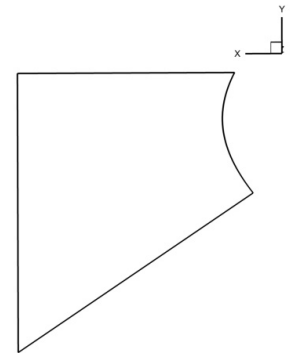
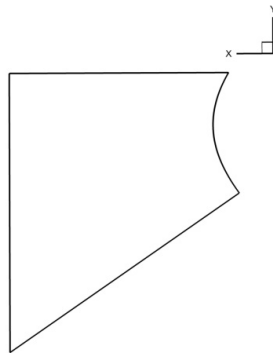
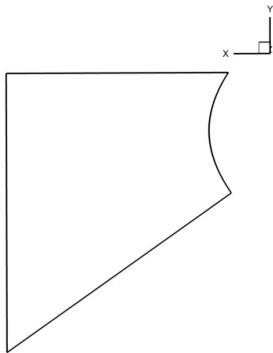


FIG. 2. Modal shape of the right-half vocal fold (Each 2D profile corresponds to mid-coronal plane).

123 where $0 \leq \beta \leq T/2$.

124 By superimposing the time-dependent displacement in Eq. (3) on the prephonatory
125 geometry, the three-dimensional shape of the glottis at any time instant can be obtained.
126 Eq. (3) is also termed as the universal kinematics equation (UKE) in this paper.

127 III. GENERALIZED GLOTTAL SHAPE LIBRARY

128 The vocal fold shape during vibration can be described by Eqs. (3) and (4) with the
129 following parameters: the vibration amplitude ξ_m , weight coefficient of mode (1, 0) α , inflec-
130 tion point factor β , phase $\phi = 12\omega t/\pi$, and ratio between the angular frequency and mucosal
131 wave speed ω/c , which is related to the vibration frequency f . The estimated physiological
132 range of these parameters for normal phonation (Smith and Titze, 2018) are listed in Table
133 I.

TABLE I. Estimated physiological range of the parameters in the UKE.

Parameters	Range
ξ_m	$(0, 0.1cm]$
α	$[0, 1]$
β	$[0, T/2]$
ϕ	$[0, 24]$
f	$[100Hz, 250Hz]$

134 In this section, we aim to verify that the UKE can be used as a generalized equation
 135 to represent any glottal shape during normal phonation. To have a good estimation of the
 136 possible glottal shapes during FSI, FSI simulations of vocal fold vibration under various
 137 subglottal pressures and material properties are conducted. The simulations employ the
 138 finite-element vocal fold model coupled with the Bernoulli equations for fast solutions (Geng
 139 *et al.*, 2016). A large number of glottal shapes are extracted from the simulation results and
 140 used to fit the UKE by using the genetic algorithm (GA) (Forrest, 1996; Goldberg, 2006;
 141 Mitchell, 1998). The fitting error is used to quantify the representative capability of the
 142 UKE. Finally, the probability density function (PDF) of each input parameter in the UKE
 143 is obtained and used to build the generalized glottal shape library through appropriate
 144 resampling.

145 A. Bernoulli-FEM FSI Simulation

146 The vocal fold tissue is modeled as the viscoelastic, transversely isotropic material. The
 147 baseline material properties of each layer of the vocal fold (Alipour *et al.*, 2000; Xue *et al.*,
 148 2012) are listed in Table II.

149 Based on the baseline material properties listed in Table II, the ranges of the material
 150 properties for each layer can be obtained by simultaneously multiplying the corresponding
 151 E_{pz}^0 and G_{pz}^0 with a factor k , where the physiological range of k is $[0.5, 5.0]$ with an increment
 152 size $\Delta k = 0.5$. Note that the value of k for the cover layer and ligament layer are always
 153 the same. The various material property factors of the cover-ligament layers and body
 154 layer under selected subglottal pressure conditions at $P_0 = 0.5kPa, 0.75kPa, 1.0kPa$ can be

TABLE II. Baseline material properties of each layer of the vocal fold.

	$\rho(g/cm^3)$	$E_p(kPa)$	ν_p	$E_{pz}^0(kPa)$	ν_{pz}	$G_{pz}^0(kPa)$
Cover	1.043	2.01	0.9	40	0.0	10
Ligament	1.043	3.31	0.9	66	0.0	40
Body	1.043	3.99	0.9	80	0.0	20

ρ is the tissue density; E_p and E_{pz}^0 are the transversal and longitudinal Youngs Modulus, respectively; ν_p and ν_{pz} are the in-plane transversal and longitudinal Poisson ratio, respectively; G_{pz}^0 is the longitudinal shear modulus (Alipour *et al.*, 2000; Xue *et al.*, 2012).

155 respectively expressed as

$$k_{CL} = m\Delta k, \quad m = 1, 2, \dots, 10, \quad (5)$$

156

$$k_B = n\Delta k, \quad n = 1, 2, \dots, 10, \quad (6)$$

157 where the subscript CL and B indicate the cover-ligament layers and body layer, respectively.

158 By systematically varying k_{CL} , k_B and P_0 , a total of 300 cases are generated for the

159 FSI simulations. For each case, the density and kinematic viscosity of the air are $1.145 \times$

160 $10^{-3}g/cm^3$ and $\nu = 1.655 \times 10^{-1}cm^2/s$, respectively. The glottis are discretized with $N_S = 69$

161 uniformly spaced cross sections along the inferior-superior direction such that the spacing

162 is 0.01cm . The contact surface is calculated as an average of the left and right surface
 163 coordinates. A uniform Rayleigh damping factor is used for each case. As an example, the
 164 vibration pattern of the vocal folds during one converged cycle at $P_0 = 1.0\text{kPa}$, $k_{CL} = 1.0$,
 165 $k_B = 4.0$ is illustrated in Figure 3, where the left subfigure corresponds to the time history
 166 of the flow rate Q during one converged cycle, and the right subfigure corresponds to the
 167 glottal shape at 5 representative phases probed from the left subfigure. The vibration shows
 168 a typical alternative convergent-divergent glottal shape change.

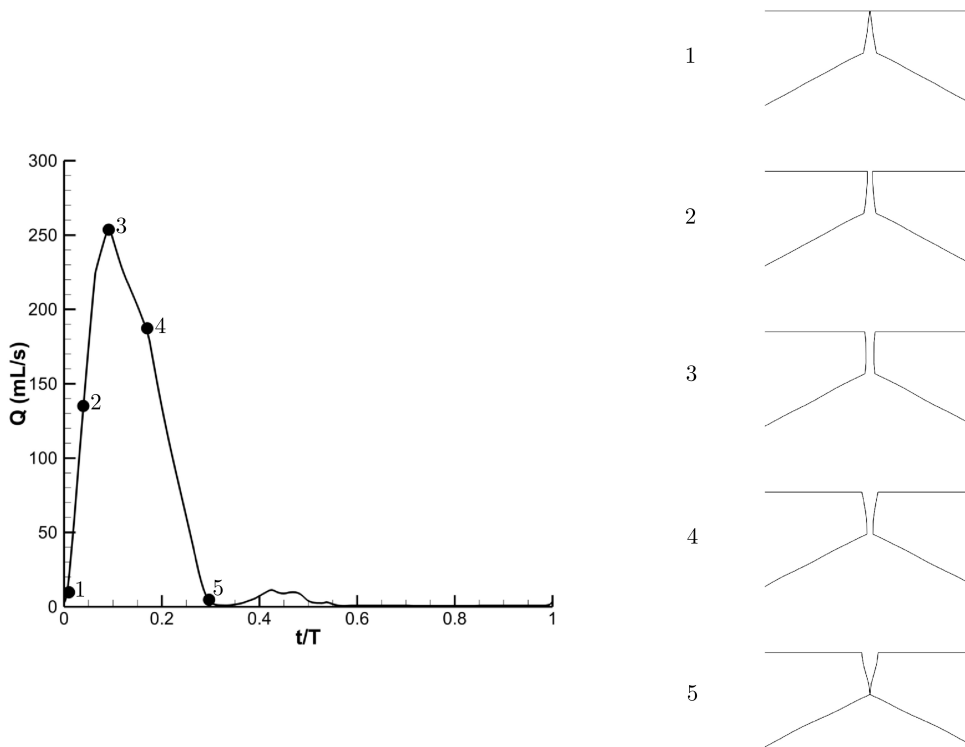


FIG. 3. Vibration pattern during one converged cycle at $P_0 = 1.0\text{kPa}$, $k_{CL} = 1.0$, $k_B = 4.0$.

B. Glottal Shape Fitting with the GA

In this subsection, we aim to verify that those glottal shapes extracted from FSI simulations in Subsection III A can be represented by the UKE. The GA is employed to inversely determine the values of the fitting parameters from the range listed in Table I such that the difference between the optimized and target (FSI) values of the nodal displacement is minimal. In the optimization process, as the flow rate heavily relies on the minimum glottal area, an equal constraint between the optimized and target minimum cross-section area along the inferior-superior direction of the glottis is enforced. Therefore, the constrained minimization function for each glottal shape can be written as,

$$\xi_m, \alpha, \beta, \phi, f = \arg \min \frac{\sum_{i=1}^n [\xi_{optimized}^i(\xi_m, \alpha, \beta, \phi, f) - \xi_{target}^i]^2}{n} \quad (7)$$

subject to $\arg \min A_j^{optimized} = \arg \min A_j^{target}, (A_j^{optimized})_{min} = (A_j^{target})_{min}$

where the values of $\xi_m, \alpha, \beta, \phi, f$ are bounded by the corresponding ranges listed in Table I, n is the number of nodal points of the glottis surface, and $A_j^{optimized}$ and A_j^{target} are the optimized and target cross-section area function with j the cross-section index, respectively. The constraints imply that the location and value of the optimized minimum cross-section area are equal to the target one.

The population size and the number of generation for the GA are chosen as 160 and 100, respectively. The overall residual of the fitness function extracted from the FSI cases in Subsection III A is plotted in Figure 4. The residual for each phase is normalized by the corresponding maximum nodal displacement. The relative residuals for most of the phases are close to 0 and the maximum relative residual among all the phases is around 0.01, indicating that GA converges well for each glottal shape and therefore the UKE can be used

189 a generalized equation to represent the extracted glottal shapes. Furthermore, the kernel
 190 density estimation (Freedman *et al.*, 2007) is used as a non-parametric way to estimate the
 191 probability density function (PDF) of the fitting parameters, and the corresponding PDF for
 192 $P_0 = 0.75kPa$ is plotted in Figure 5. The PDF for $P_0 = 0.5kPa$ and $P_0 = 1.0kPa$ are highly
 193 similar and thus not shown. Note that the PDF of the optimized frequency is not plotted
 194 in those figures because the values for all cases are similar and the corresponding PDFs are
 195 concentrated at $f = 210Hz$. Therefore, to reduce the number of redundant shapes, we fix
 196 the value of the optimized frequency to be $f = 210Hz$. Based on the PDFs, the generalized
 197 glottal shape library can be built by appropriately resampling the parameters. Concretely,
 198 we first locate the parameter values with the local maximum probabilities from each PDF,
 199 and then with this located value as the center value, conduct the uniform resampling from
 200 each PDF such that the majority of the representative glottal shapes can be included in this
 201 library. The re-sampled values of the input parameters under different subglottal pressure
 202 conditions are listed in Table III. Note that for different subglottal pressure values, only the
 203 amplitude ξ_m is different, and the other parameters are all the same. A total of $N_L = 3960$
 204 different shapes are generated by substituting the values in Table III into the UKE, and
 205 these shapes constitute the generalized glottal shape library which are used as the raw data
 206 for training the DNN in the next section.

207 IV. IMPLEMENTATION OF THE DNN MODEL

208 For each shape in the generalized glottal shape library, the subglottal pressure P_0 and
 209 the parameters ξ_m , α , β and ϕ are the input features, and the corresponding output targets

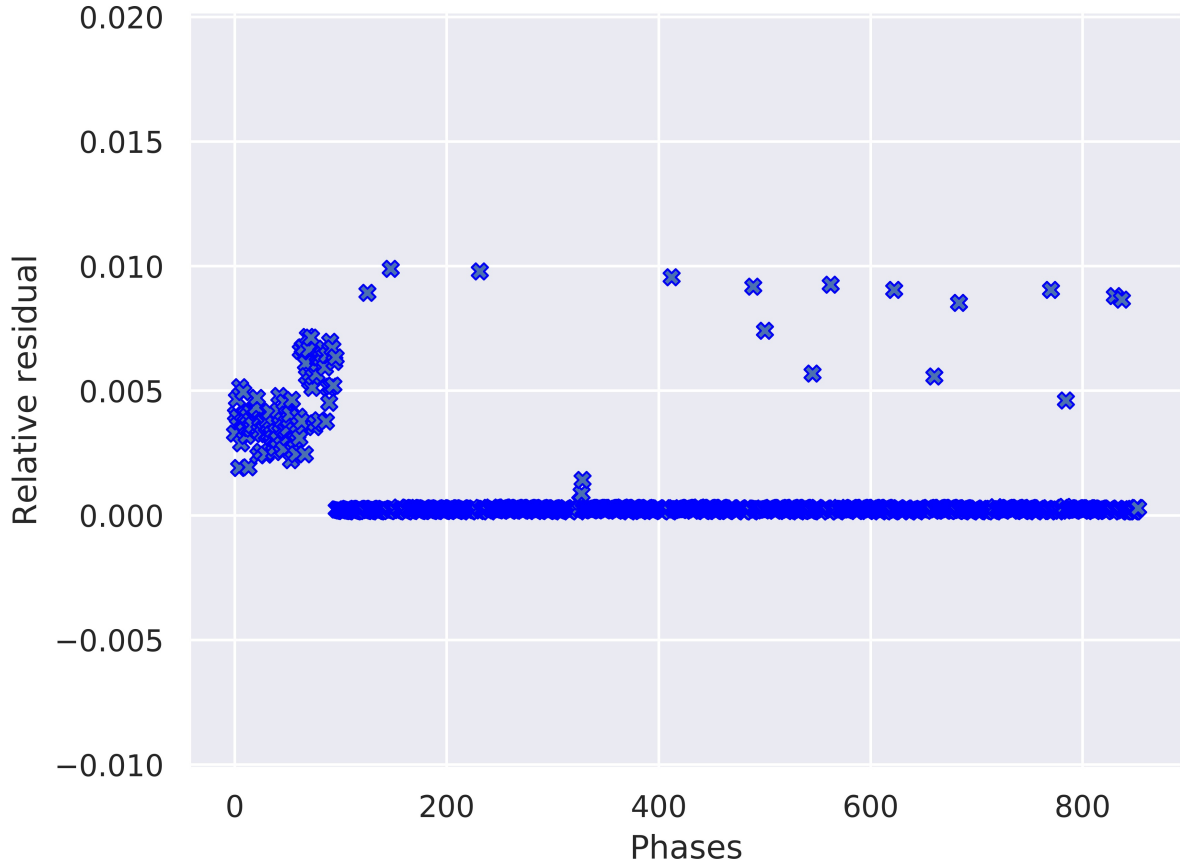


FIG. 4. Relative residual of the fitness function of GA.

210 are the flow rate Q and the pressure distribution P_i , where i is the index of the discretized
 211 cross sections in the inferior-superior direction of the vocal folds. The ground truth values
 212 of the flow rate Q and pressure distribution P_i are obtained by solving the N-S equations.
 213 Then, the mapping relationship between the input features and the corresponding output
 214 targets can be established by a fully-connected DNN as follows:

$$Q, P_i = f(P_0, \xi_m, \alpha, \beta, \phi; \theta) \quad (8)$$

TABLE III. Resampled values of input parameters.

$P_0(kPa)$	ξ_m	α	β	ϕ
0.5	0.02, 0.03,			
	0.04, 0.1			1, 2, 3, 4,
0.75	0.025, 0.04,	0.0, 0.2, 0.4, 0.0, 0.015, 0.03,		5, 6, 7, 8,
	0.055, 0.1	0.6, 0.8, 1.0	0.135, 0.15	9, 10, 11
1.0	0.035, 0.055,			
	0.075, 0.1			

215 where f is the function representing the overall DNN, and θ denotes all learnable parameters
 216 of the DNN. With this trained DNN, the flow rate and pressure distribution along any glottal
 217 shape generated by the UAE can be well predicted.

218 A. N-S Solution of the Output Targets

219 The fluid flow is governed by the incompressible N-S equations as follows,

$$\frac{\partial u_i}{\partial x_i} = 0 \quad (9)$$

$$\frac{\partial u_i}{\partial t} + \frac{\partial u_i u_j}{\partial x_j} = -\frac{1}{\rho_f} \frac{\partial p}{\partial x_i} + \nu_f \frac{\partial^2 u_i}{\partial x_j \partial x_j}, \quad (10)$$

220 where u_i , ρ , p , ν are the incompressible flow velocity, density, pressure, and kinematic vis-
 221 cosity, respectively. An in-house sharp-interface immersed-boundary N-S flow solver (Zheng
 222 *et al.*, 2010) is used to obtain the ground truth solution of the output targets. The setup of

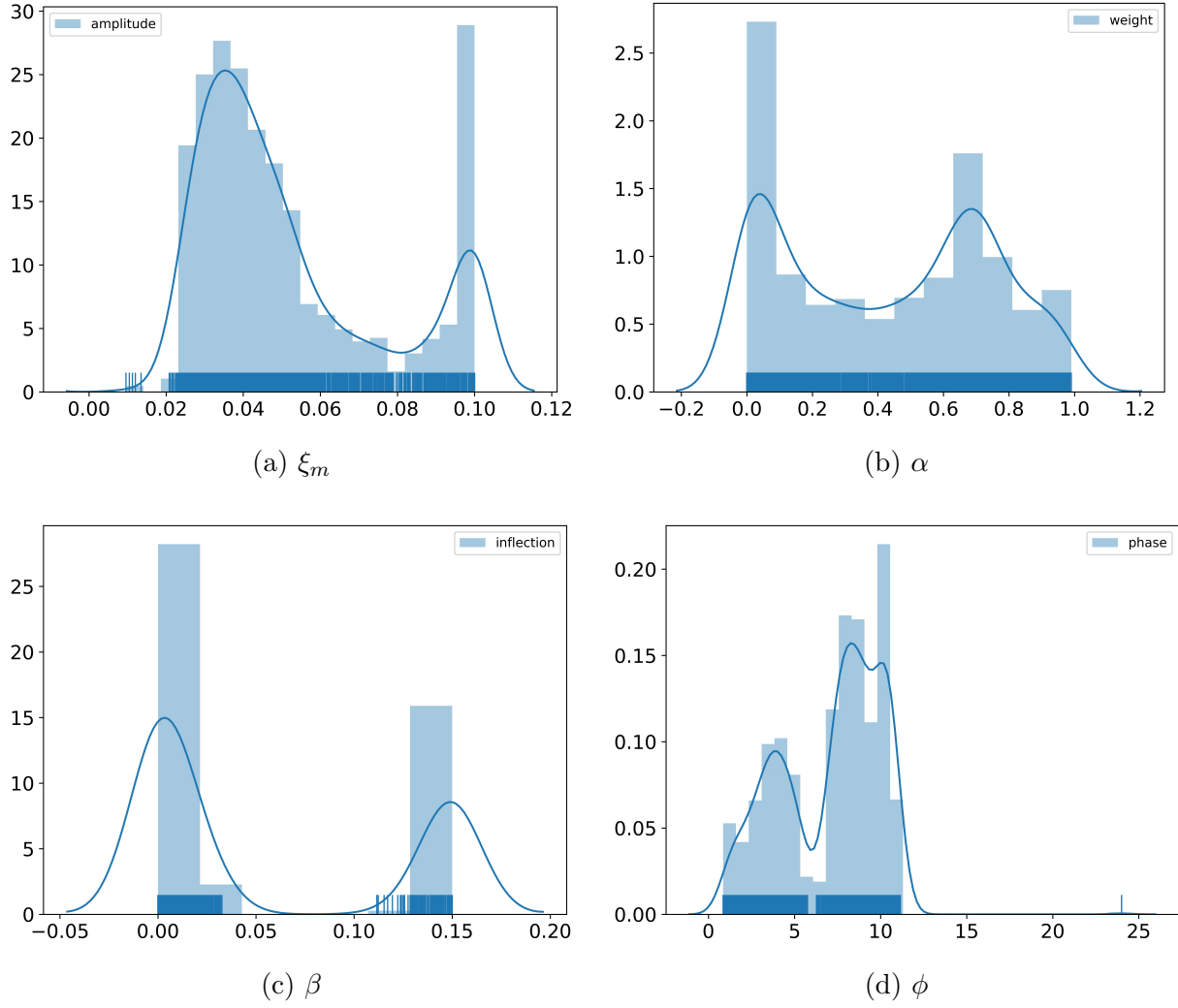


FIG. 5. PDF of optimized input parameters for $P_0 = 0.75kPa$.

223 the computational domain is depicted in Figure 6. The size of the computational domain is
 224 $1.5\text{cm} \times 21.0\text{cm} \times 1.5\text{cm}$ in the x (lateral), y (inferior-superior) and z (anterior-posterior)
 225 direction. The vocal folds are placed 3.2cm and 17.0cm away from the inlet and outlet of the
 226 computational domain, respectively. The grid independence study is performed by compar-
 227 ing the flow rate and average pressure distribution on coarse, medium and fine meshes with
 228 fixed CFL number. The mesh number $N_x \times N_y \times N_z$ on the coarse, medium and fine meshes
 229 are $64 \times 64 \times 24$, $128 \times 128 \times 48$, and $256 \times 256 \times 96$ in the x , y and z direction, respectively,
 230 where N_x , N_y and N_z are the number of mesh nodes in the x , y and z direction, respectively.
 231 The mesh is stretched to the far field in the x and y direction, while uniformly distributed
 232 in the z direction. The grid independence results of the flow rate and average pressure dis-
 233 tribution are illustrated in Figure 7. From this figure, we can see that the medium mesh is
 234 adequate to obtain the ground truth solution of the output targets from the shape library.
 235 The relative error of the flow rate obtained on the coarse and medium mesh with respect to
 236 that obtained on the fine mesh are 12.1% and 1.0%, respectively. The minimum interval of
 237 the medium mesh is 0.003cm and 0.01cm in the x and y direction, respectively. Moreover,
 238 the total CPU time required for convergence on the coarse, medium and fine meshes are
 239 respectively 0.2, 2.3 and 35 hours on a parallel computer with 32 CPUs.

240 B. Implementation Details of the DNN

241 As mentioned above, the input features and corresponding output targets extracted from
 242 the shape library can be organized as a vector \mathbf{x} and \mathbf{y} , respectively,

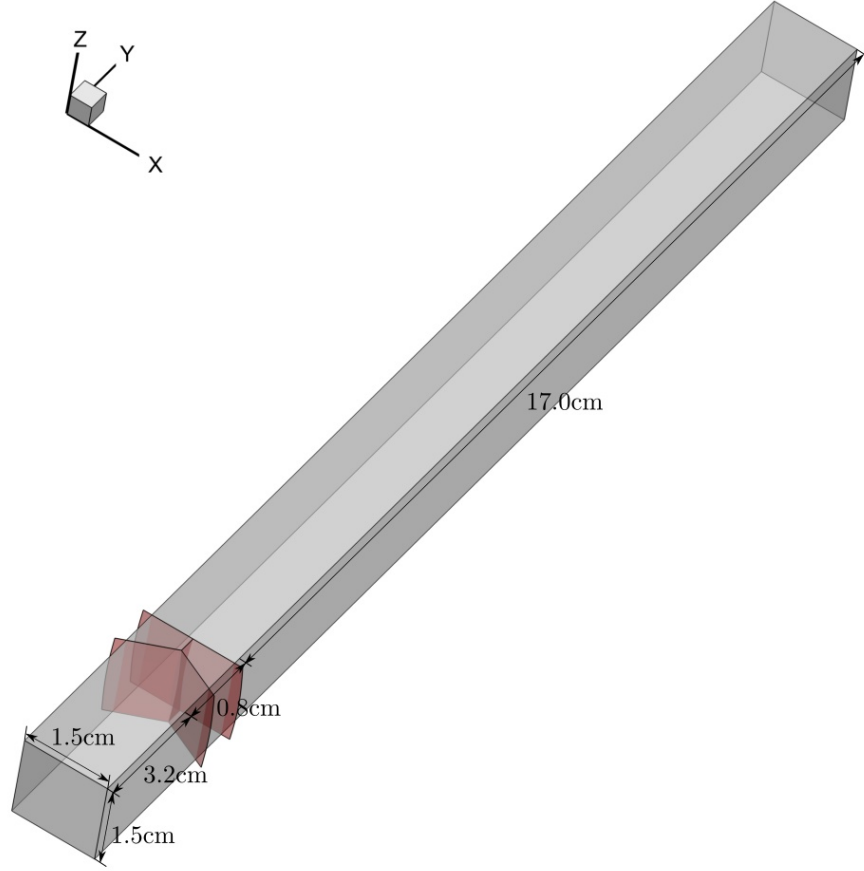


FIG. 6. Setup of the computational domain.

$$\mathbf{x} = \begin{bmatrix} P_0 \\ \xi_m \\ \alpha \\ \beta \\ \phi \end{bmatrix}, \quad \mathbf{y} = \begin{bmatrix} Q \\ P_1 \\ P_2 \\ \vdots \\ \vdots \\ P_{N_P} \end{bmatrix}, \quad (11)$$

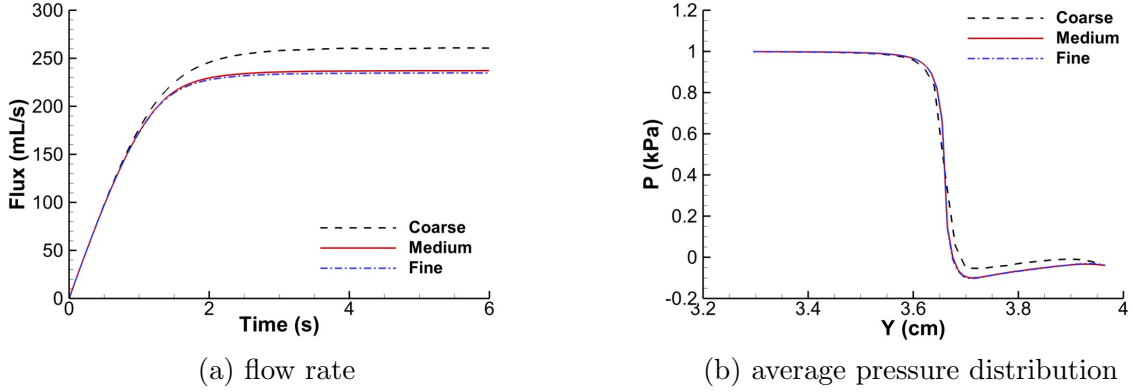


FIG. 7. Grid independence results.

243 where $N_P = 68$ is the dimension of the output pressure distribution.

244 The mapping relationship between the input features \mathbf{x} and corresponding output targets
 245 \mathbf{y} can be established by a fully-connected DNN (Goodfellow *et al.*, 2016; LeCun *et al.*,
 246 2015). In the fully-connected DNN, the input and output layers are denoted as \mathbf{z}_0 and \mathbf{z}_L ,
 247 respectively. The layers between the input and output layers are called the hidden layers \mathbf{z}_l ,
 248 where $l = 1, \dots, L - 1$. Neurons in the hidden layer \mathbf{z}_l have connections to all neurons of the
 249 previous layer \mathbf{z}_{l-1} ,

$$\mathbf{z}_l = \sigma_l(\mathbf{W}_l^T \mathbf{z}_{l-1} + \mathbf{b}_l) \quad (12)$$

250 where \mathbf{W}_l is the learnable weights, \mathbf{b}_l is the additive bias, and σ_l is the nonlinear activation
 251 function.

252 The loss function J of the DNN is

$$J = \frac{1}{N} \sum \|\mathbf{z}_L - \mathbf{y}\|_2^2 + \lambda \|\mathbf{W}\|_2 \quad (13)$$

253 where \mathbf{z}_L is the predicted value and λ is the regularization coefficient to prevent the overfit-
 254 ting of the DNN model.

255 Note that the range of values of Q and P_i are different, i.e., $Q \geq 0$ while $P_i/P_0 \leq 1$,
256 therefore for the ease of training the DNN, the input features \mathbf{x} are respectively mapped to
257 the subsets of the output targets \mathbf{y} (i.e., Q and P_i) with different architectures of the DNN.

258 The whole data set from the shape library is randomly split into the training and test
259 sets. To avoid the overfitting of the model, we use 5-fold cross validation (Goodfellow *et al.*,
260 2016) to fine tune the architecture and hyperparameters of the DNN, such as the number of
261 hidden layers, the number of neurons on each hidden layer, the initialization of the weights,
262 the activation function, the optimization method, the mini-batch size, and the number of
263 epochs (Goodfellow *et al.*, 2016). The final architecture and hyperparameters of the DNN
264 are chosen from those that have the lowest errors on the validation set. The final DNN
265 model is then trained on the full training set, and the prediction performance of the trained
266 model is evaluated on the test set.

267 The final architectures of the DNN for Q and P_i are illustrated in Figure 8 and denoted
268 as DNN-Q and DNN-P, respectively. The input layer for both DNNs has 5 neurons which
269 correspond to the dimension of the input vector. The output layer of DNN-Q has a single
270 neuron which corresponds to the ground truth value of the flow rate Q , while that of DNN-P
271 has 68 neurons which correspond to the ground truth value of the pressure distribution on
272 the discretized cross sections along the inferior-superior direction of the vocal folds. Since
273 Q and P_i are bounded by different ranges ($Q \geq 0$ and $P_i/P_0 \leq 1$), the softplus and tanh
274 activation function (Goodfellow *et al.*, 2016) are used on the output layer of DNN-Q and
275 DNN-P, respectively. Besides the input layer and output layer, there are two hidden layers
276 for both DNNs. The number of neurons on the hidden layers of DNN-Q are 64, and the

277 softplus activation function is used on each hidden layer, whereas the number of neurons on
 278 the hidden layers of DNN-P are 256, and the relu activation function (Goodfellow *et al.*, 2016)
 279 is used on each hidden layer. All of the weights on each layer are initialized with a random
 280 normal distribution. Both of the DNN models are optimized using a mean-squared loss
 281 function with an adaptive version of the stochastic gradient descent algorithm called Nadam
 282 (Nesterov Adam) (Ruder, 2016). Both of the DNN models are trained with 10000 epochs,
 283 where one epoch consists of one full training cycle on the training set, and the mini-batch
 284 size is 128 for each epoch. The DNN models are implemented on the open-source machine
 285 learning platform Keras (Chollet *et al.*, 2015) using TensorFlow (Abadi *et al.*, 2015) as the
 286 backend.

287 C. Evaluation of the Trained DNN Models

288 The relative percent difference (RPD) between the true and predicted outcomes is used
 289 to evaluate the trained DNN models. The expression of the RPD for Q and P_i for each
 290 glottal shape in the training data are as follows:

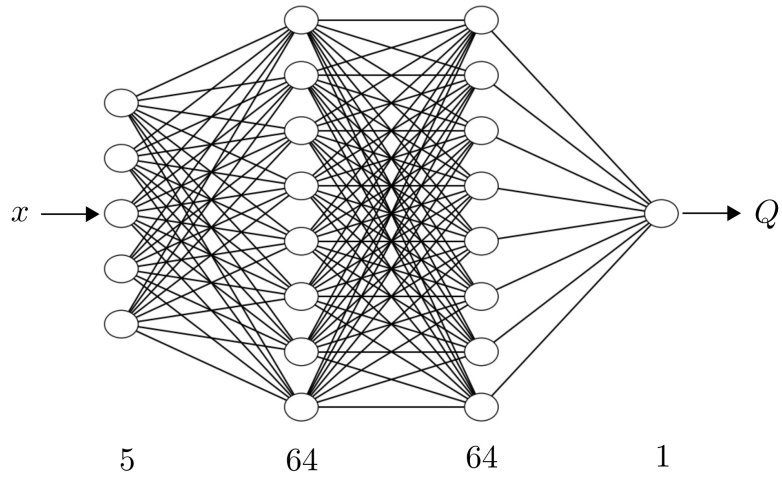
$$E_Q = \frac{|Q - \hat{Q}|}{\max(|Q|, |\hat{Q}|)} \quad (14)$$

291

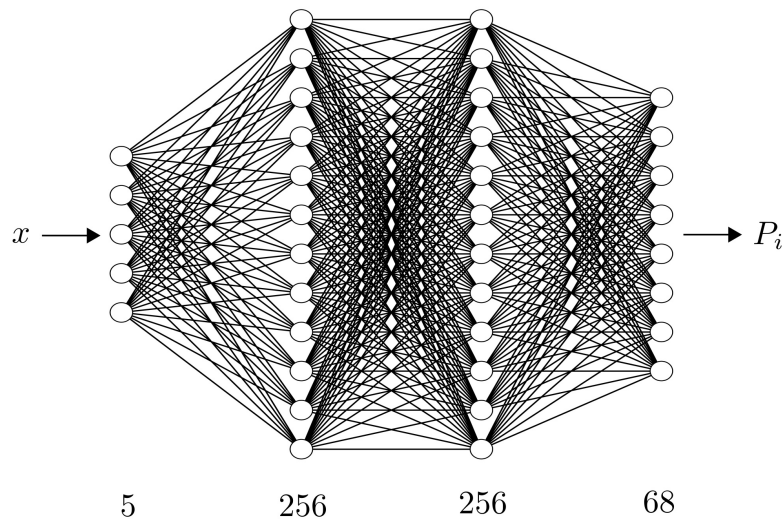
$$E_P = \frac{\sum_{i=1}^{N_P} \frac{|P_i - \hat{P}_i|}{\max(|P_i|, |\hat{P}_i|)}}{N_P} \quad (15)$$

292 where Q , P_i and \hat{Q} , \hat{P}_i are respectively the true and predicted outcomes.

293 The history of the 5-fold cross validation results for DNN-Q and DNN-P is plotted in
 294 Figure 9. The horizontal axis corresponds to the number of epochs, and the vertical axis



(a) DNN-Q



(b) DNN-P

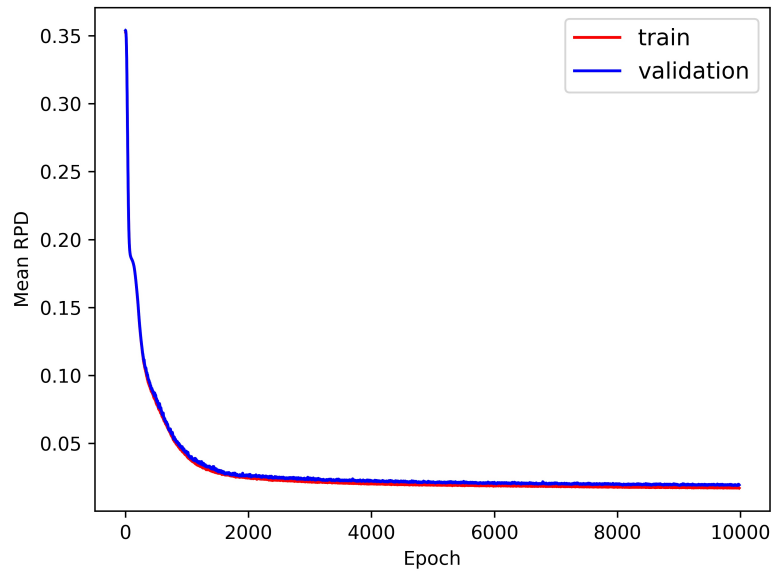
FIG. 8. Architecture of the DNN.

295 corresponds to the mean RPD between the true and predicted outcomes. The comparison
 296 is between the training and validation sets. It took 10000 epochs for the mean RPD on
 297 the training and validation sets to converge for DNN-Q and DNN-P. The converged mean
 298 RPD on the training and validation sets are 1.71% and 1.89% for DNN-Q, and 1.97% and
 299 4.12% for DNN-P, respectively. The performance of the trained DNN-Q and DNN-P on
 300 the test set is plotted in Figure 10 and 11, respectively. The first subfigure for each figure
 301 shows the history of the model accuracy where the horizontal and vertical axes correspond
 302 to the number of epochs and mean RPD, respectively. The comparison is between the full
 303 training and test sets. After running 10000 epochs, the mean RPD on the test set converges
 304 at 1.74% and 3.52% for DNN-Q and DNN-P, respectively. The second subfigure illustrates
 305 the scatter plot of the true and predicted outcomes on the test set, and the good prediction
 306 performance on the test set for both DNN-Q and DNN-P can be observed. The final mean
 307 RPD on the training, validation and test sets for DNN-Q and DNN-P are summarized in
 308 Table IV.

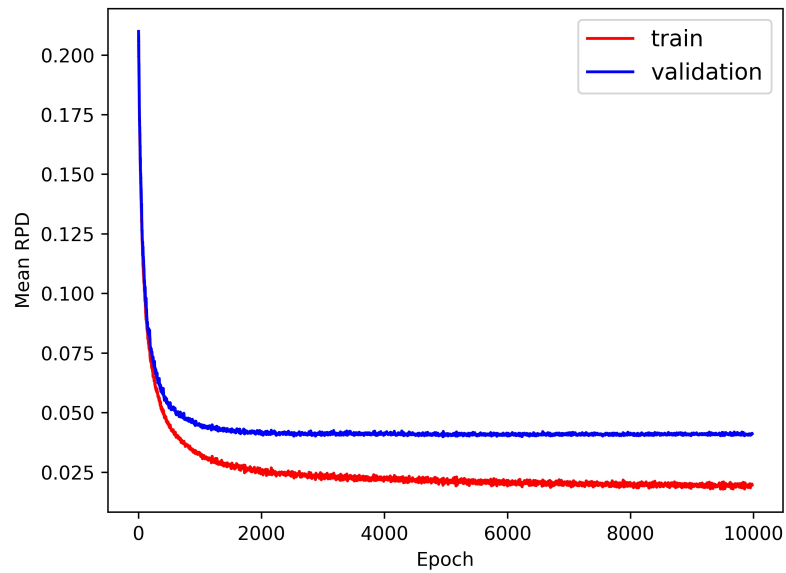
TABLE IV. Mean RPD on the training, validation and test sets.

	train	validation	test
Q	1.71%	1.89%	1.74%
P_i	1.97%	4.12%	3.52%

309 Furthermore, 6 shapes under different subglottal pressures are randomly selected from the
 310 test set, and the comparison of the true and predicted pressure distribution of these shapes

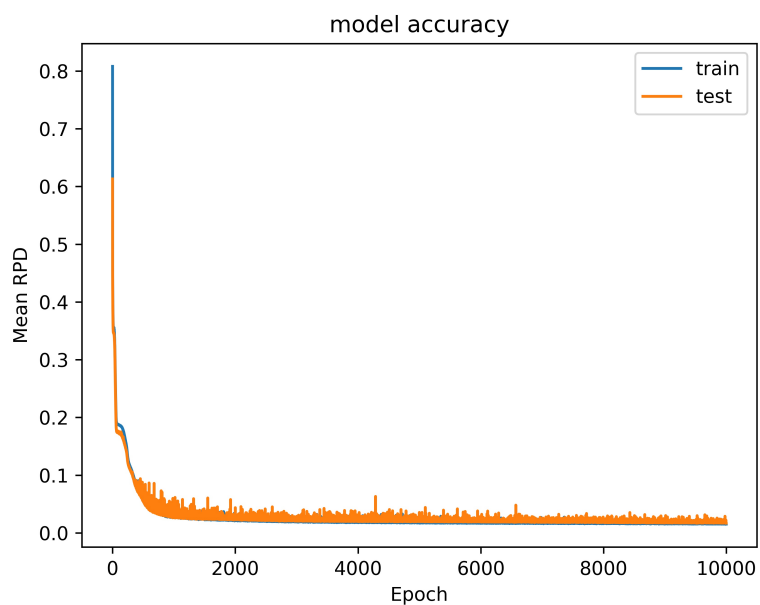


(a) DNN-Q

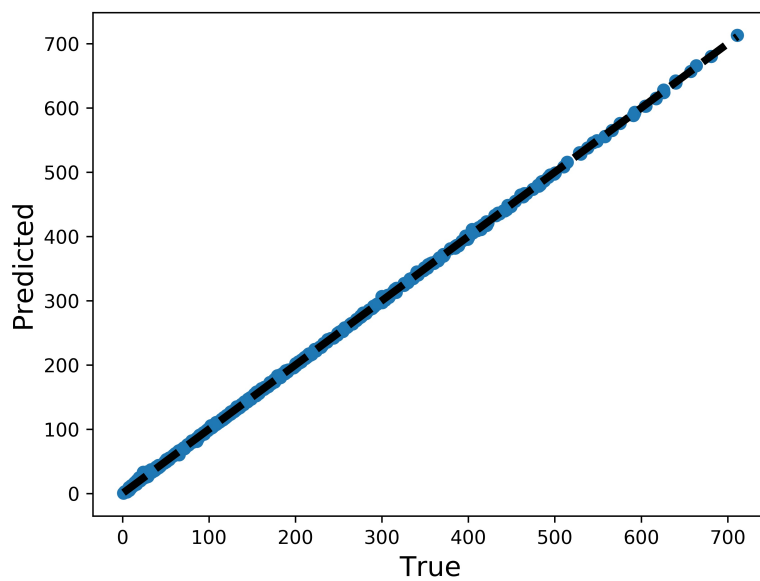


(b) DNN-P

FIG. 9. 5-fold cross validation results.

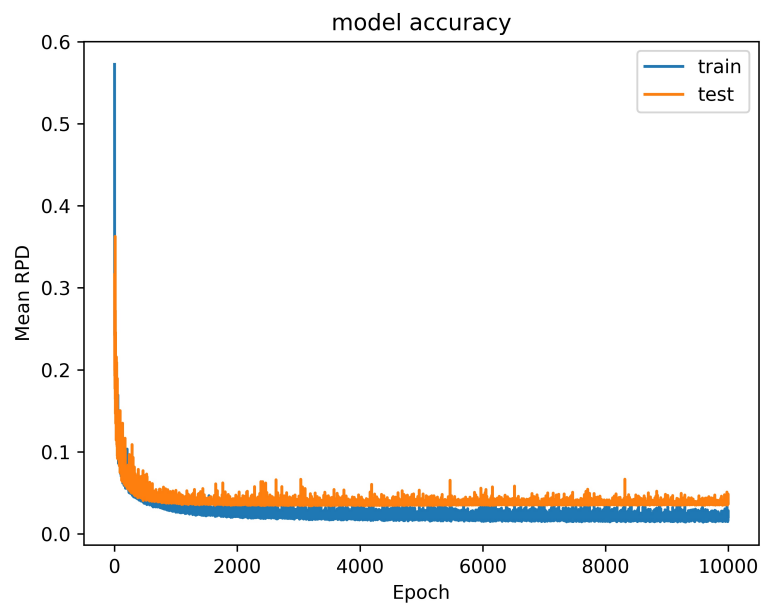


(a) History of the model accuracy

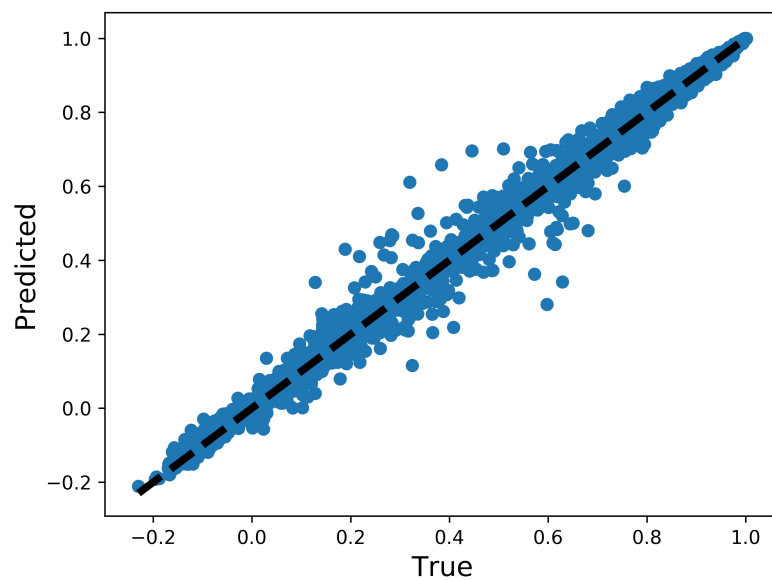


(b) Scatter plot

FIG. 10. Performance of the trained DNN-Q model on the test set.



(a) History of the model accuracy



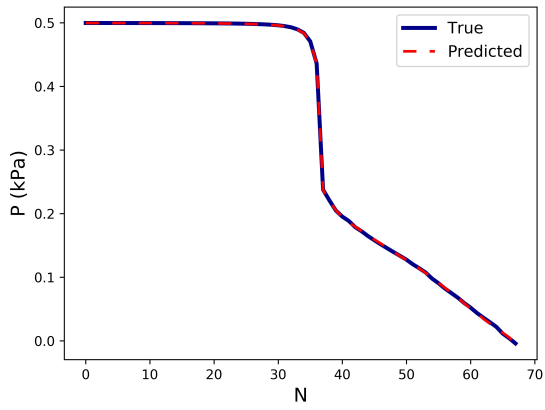
(b) Scatter plot

FIG. 11. Performance of the trained DNN-P model on the test set.

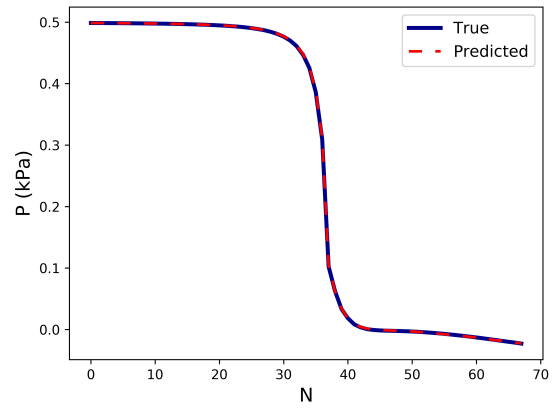
311 are shown in Figure 12. From these figures, we can observe that the pressure distribution
312 can be well predicted by the trained DNN-P model.

313 To summarize, the diagram of the implementation of the present reduced-order flow solver
314 is illustrated in Figure 13. Concretely, it is divided into the following steps: firstly, various
315 glottal shapes are extracted from 300 converged Bernoulli-FEM FSI results under different
316 subglottal pressure and material properties. Secondly, these extracted shapes are fitted
317 with the UKE using the GA and the PDF of the fitted input parameters of the UKE are
318 determined. Thirdly, 3960 different glottal shapes are generated by appropriate resampling
319 from the PDF of the input parameters with high probabilities and then substituting them
320 into the UKE, which constitute the generalized shape library. Fourthly, for each shape in
321 the library, the ground truth values of the flow rate Q and pressure distribution P_i are
322 obtained by solving the N-S equation. Finally, the mapping relationship between the input
323 parameters together with the subglottal pressure (input features) and the corresponding
324 flow rate and pressure distribution along the inferior-superior direction of the glottal shape
325 (output targets) are established by the fully-connected DNN. With this reduced-order flow
326 solver, for any glottal shape, the input features can be extracted from the UKE with the
327 GA and then the flow rate and pressure distribution can be predicted with the trained
328 DNNs. The implementation procedure of the reduced-order flow solver can be summarized
329 in Algorithm 1.

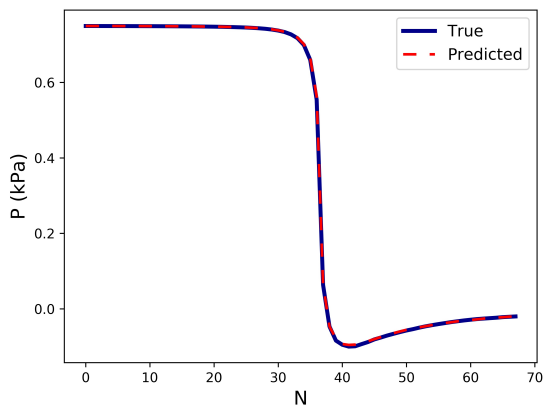
330 The developed reduced-order flow model is then coupled with the FEM based solid dy-
331 namics solver for FSI simulation. The abstract workflow of the ROM for FSI simulation
332 is illustrated in Figure 14. First, the flow rate Q and pressure distribution P_i of the glot-



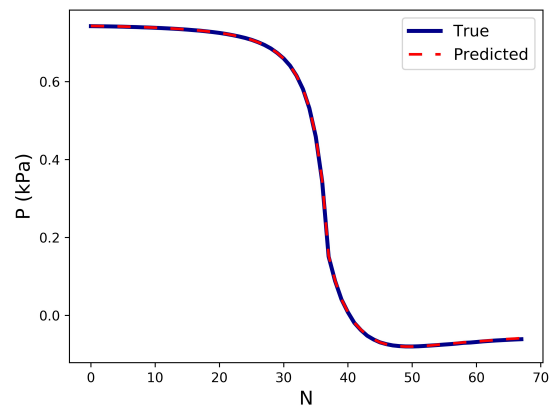
(a)



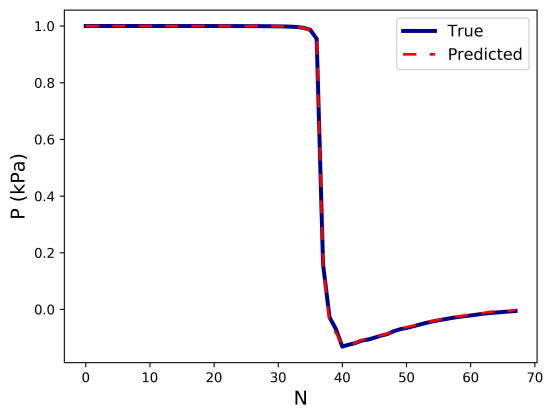
(b)



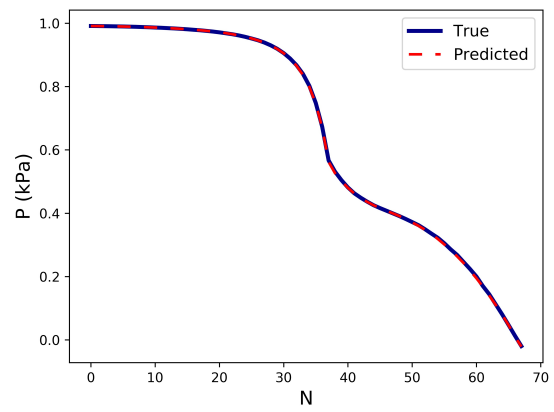
(c)



(d)



(e)



(f)

FIG. 12. Comparison of the true and predicted pressure distribution.

333 tal shape X at a certain time instant t can be obtained by the present reduced-order flow
 334 solver, then the pressure load is fed into the FEM solid solver to calculate the corresponding
 335 deformation of the glottis ΔX , finally the updated glottal shape $X + \Delta X$ is used as the
 336 initial shape of the glottis at the next time instant $t + \Delta t$. The reduced-order flow solver
 337 and FEM based solid solver are coupled in a weak manner.

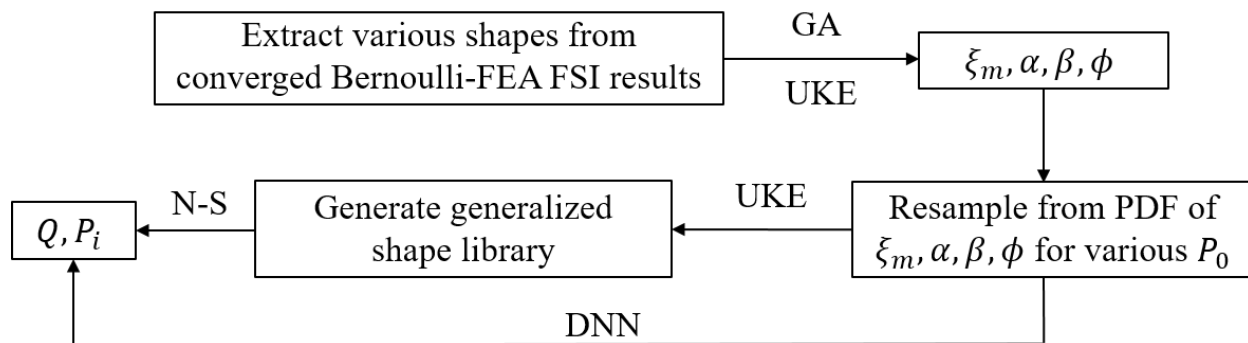


FIG. 13. Diagram of the implementation of the reduced-order flow solver.

Algorithm 1: Implementation of the reduced-order flow solver

- 1 Extract various shapes from converged Bernoulli-FEA FSI results;
 - 2 Fit these extracted shapes with the UKE using the GA;
 - 3 Obtain the PDF of the fitted parameters of the UKE: ξ_m, α, β and ϕ ;
 - 338 4 Resample the PDF of ξ_m, α, β and ϕ for various P_0 ;
 - 5 Substitute the resampled values into the UKE to generate the generalized shape library;
 - 6 Obtain the ground-truth values of Q and P_i for each shape in the library;
 - 7 Establish the mapping relationship Eq.(8) with a fully-connected DNN
-

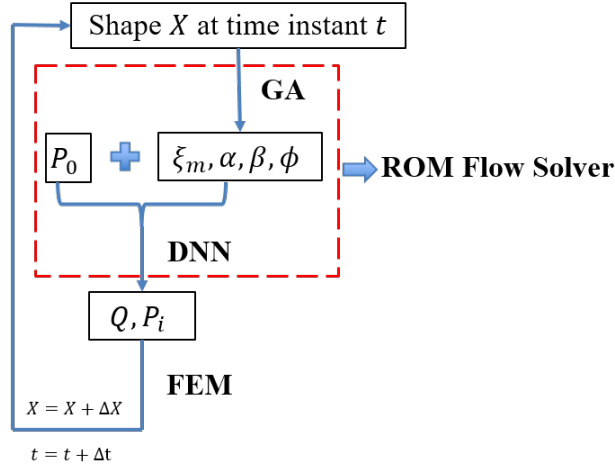


FIG. 14. Workflow of the reduced-order model for FSI simulation.

339 **V. EVALUATION OF THE PERFORMANCE OF THE GENERALIZED ROM**
 340 **FOR FSI SIMULATION**

341 To evaluate the prediction performance of the present generalized ROM for FSI sim-
 342 ulation, the ROM-FSI results are first compared with the FOM quasi-static (QS) results
 343 and the correlation and agreement between these results are analyzed, and then compared
 344 with the FOM-FSI results in terms of the voice quality-related parameters and CPU time.
 345 Detailed discussions are given as below.

346 **A. Comparison with FOM-QS Results**

347 A series of new subglottal pressure and material properties are simulated using the ROM-
 348 FSI model to generate the glottal shapes that are not in the shape library and evaluate the
 349 corresponding prediction performance. The values of the selected subglottal pressure and
 350 material properties are listed in Table V. The simulation setup is the same as described

351 in Subsection III A. An example of the converged time history of the flow rate Q at $P_0 =$
 352 $0.8kPa$, $k_{CL} = 4.75$, $k_B = 3.75$ predicted by the ROM is illustrated in Figure 15. Note that
 353 some fluctuations at the end of the closing phase can be observed, and this is likely due to
 354 the unsatisfactory representation of these shapes by the UKE due to the contact issue.

TABLE V. Selected subglottal pressure and material properties for evaluation.

P_0 (kPa)	k_{CL}	k_B
0.625		
0.7	1.75, 2.75, 3.75, 4.75	1.75, 3.75
0.8		
0.875		

355 Various glottal shapes are extracted from the converged FSI results of the cases listed
 356 in Table V. By excluding the fully-closed and nearly-closed shapes which may not be well
 357 represented by the UKE due to the contact issue, the total number of the extracted shapes
 358 for evaluation is 1582.

359 For each FSI case n in Table V, at each time step of the steady-cycle ROM-FSI result,
 360 the flow rate $Q_{ROM}^{n,k}$ and pressure distribution $P_{i,ROM}^{n,k}$ are respectively extracted, and the
 361 corresponding reference values of $Q_{FOM}^{n,k}$ and $P_{i,FOM}^{n,k}$ can be computed by the FOM, where
 362 k is the index of the time step for each case. The time-averaged error of Q and P_i for each
 363 FSI case, designated as E_Q^n and E_P^n , can be calculated as follows:

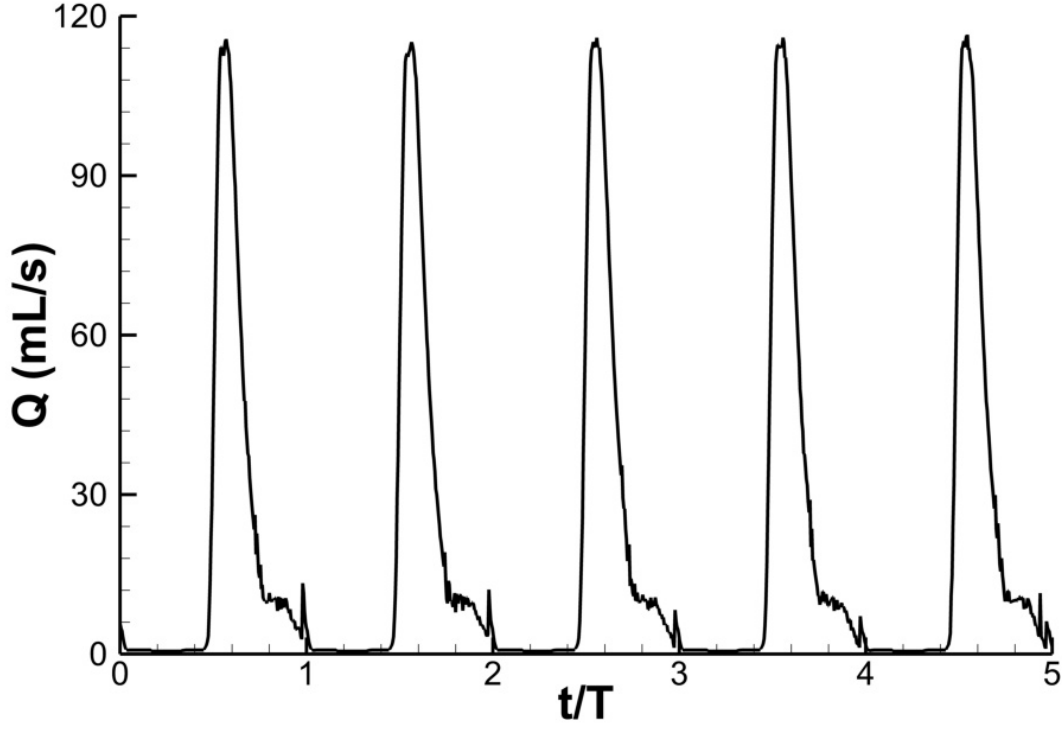


FIG. 15. Example of the converged time history of the predicted flow rate Q at $P_0 = 0.8kPa$,
 $k_{CL} = 4.75$, $k_B = 3.75$.

$$E_Q^n = \frac{1}{n_t \bar{Q}_{FOM}^n} \sum_{k=1}^{n_t} |Q_{FOM}^{n,k} - Q_{ROM}^{n,k}| \quad (16)$$

$$E_P^n = \sum_{k=1}^{n_t} \sum_{i=1}^{N_P} \frac{|P_{i,FOM}^{n,k} - P_{i,ROM}^{n,k}|}{P_0} \quad (17)$$

364 where n_t and \bar{Q}_{FOM}^n are the number of extracted time instants and the time-averaged refer-
 365 ence values of the flow rate for each case, respectively.

366 The overall average error of Q and P_i , designated as E_Q and E_P , can be calculated as:

$$E_Q = \frac{1}{n_c} \sum_{n=1}^{n_c} E_Q^n \quad (18)$$

$$E_P = \frac{1}{n_c} \sum_{n=1}^{n_c} E_P^n \quad (19)$$

367 where n_c is the number of cases listed in Table V. The overall average error of Q and P_i are
 368 7.87% and 1.68%, respectively.

369 Additionally, the correlation and agreement between the true and predicted Q and P_i
 370 for the extracted 1582 glottal shapes are quantified. In terms of Q , the Pearson corre-
 371 lation coefficient (Freedman *et al.*, 2007) between Q_{FOM} and Q_{ROM} is excellent (0.993,
 372 $P < 0.0005$). The scatter and correlation plots are also depicted in Figure 16, where the
 373 horizontal and vertical axes correspond to the true (Q_{FOM}) and predicted (Q_{ROM}) val-
 374 ues, respectively. The Bland-Altman plot (Altman and Bland, 1983) is used to analyze
 375 the agreement between Q_{FOM} and Q_{ROM} . The result is plotted in Figure 17. As can be
 376 seen from this figure, the mean difference between Q_{FOM} and Q_{ROM} is $-2.784mL/s$, and
 377 the 95% limits of agreement (LoA) between them is from $-12.505mL/s$ to $6.936mL/s$.
 378 The 95% confidence interval (CI) of the mean difference, upper LoA and lower LoA be-
 379 tween Q_{FOM} and Q_{ROM} is $[-3.0288mL/s, -2.5401mL/s]$, $[6.5177mL/s, 7.3539mL/s]$ and
 380 $[-12.9288mL/s, -12.0866mL/s]$, respectively. The number of the outliers is 38, and the
 381 percentage of the outliers is 2.40%.

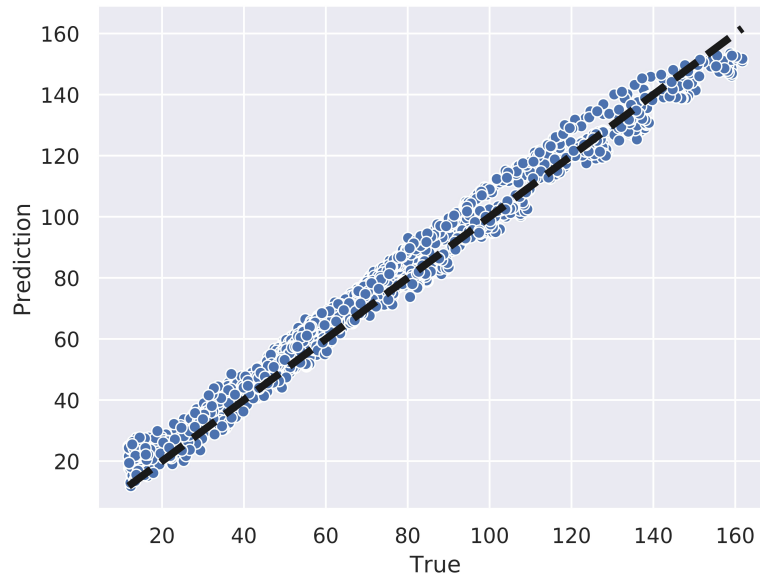
382 Similarly, in terms of P_i , the Pearson correlation coefficient between $P_{i,FOM}$ and $P_{i,ROM}$
 383 is excellent (0.997, $P < 0.0005$). The scatter and correlation plots are also depicted in
 384 Figure 18, where the horizontal and vertical axes correspond to the true ($P_{i,FOM}$) and

385 predicted ($P_{i,ROM}$) values, respectively. The Bland-Altman analysis between $P_{i,FOM}$ and
386 $P_{i,ROM}$ is plotted in Figure 19. From this figure, we can observe that the mean differ-
387 ence between $P_{i,FOM}$ and $P_{i,ROM}$ is $0.006kPa$, and the 95% LoA between them is from
388 $-0.011kPa$ to $0.023kPa$. The 95% CI of the mean difference, upper LoA and lower
389 LoA between $P_{i,FOM}$ and $P_{i,ROM}$ is $[0.0053kPa, 0.0062kPa]$, $[0.0218kPa, 0.0232kPa]$ and
390 $[-0.0117kPa, -0.0103kPa]$, respectively. The number of the outliers is 87, and the percent-
391 age of the outliers is 5.50%.

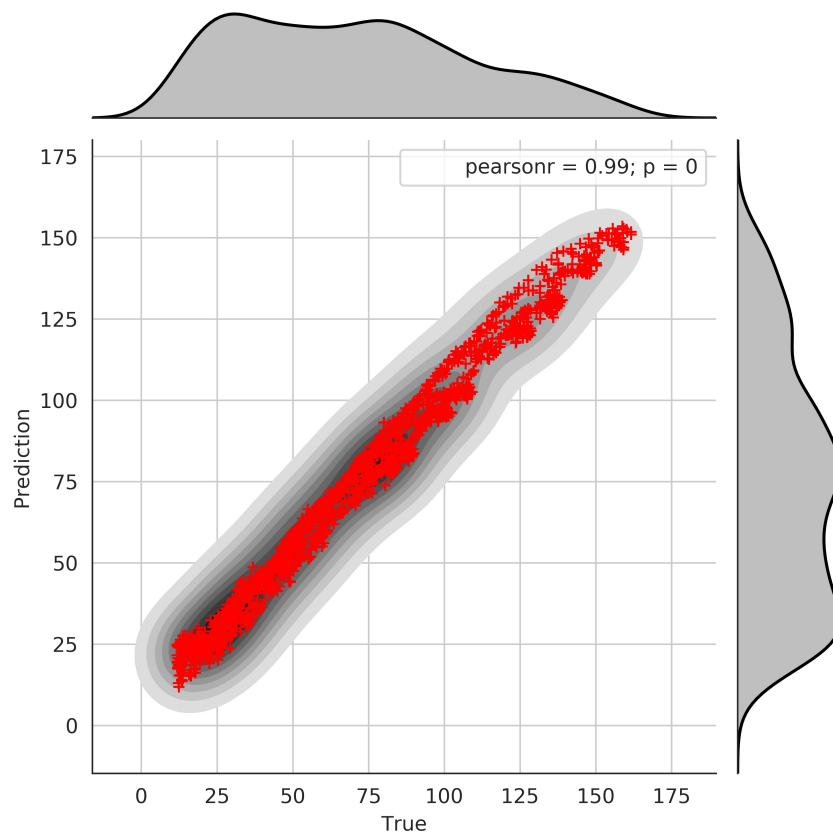
392 The above correlation and agreement analysis results between the true and predicted Q
393 and P_i for various glottal shapes indicate that the present ROM-FSI results agree very well
394 with the corresponding FOM-QS results.

395 B. Comparison with FOM-FSI Results

396 FSI simulations at $P_0 = 0.8kPa$, $k_{CL} = 1.75$, $k_B = 3.75$ (Case 1) and $P_0 = 0.875kPa$,
397 $k_{CL} = 3.75$, $k_B = 3.75$ (Case 2) from Table V are conducted by using both the ROM-FSI
398 model and FOM-FSI model. The comparison of the phase-averaged time history of the
399 flow rate Q for both cases are illustrated in Figure 20. From this figure, we can observe
400 that the peak flow rate, mean flow rate and the fundamental frequency are close to each
401 other while the skewing of the waveform is different. Several important voice quality-related
402 parameters (Xue *et al.*, 2014) are computed from Figure 20 for both of the cases and the
403 corresponding phase-averaged values are listed in Table VI. It can be seen from this table
404 that the overall agreement between the values obtained by the ROM-FSI and FOM-FSI is
405 satisfactory. The relative errors δ of F_0 , Q_{max} , Q_{mean} and ξ_m between the ROM-FSI and



(a) Scatter plot



(b) Correlation plot

FIG. 16. Scatter and correlation plot of Q .

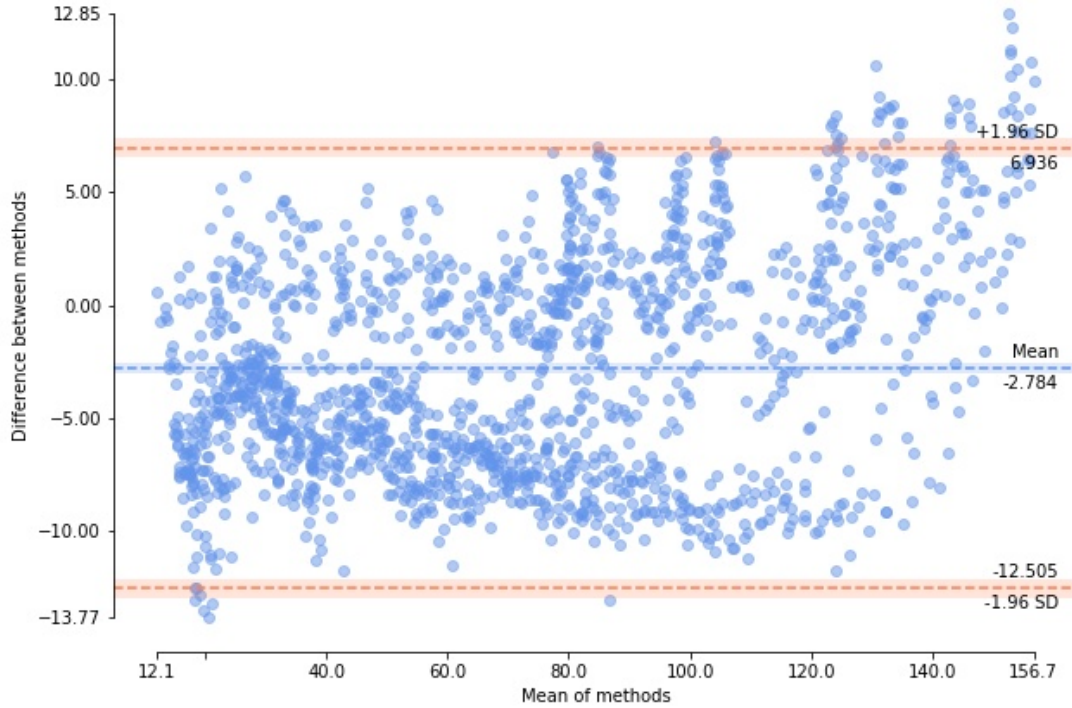
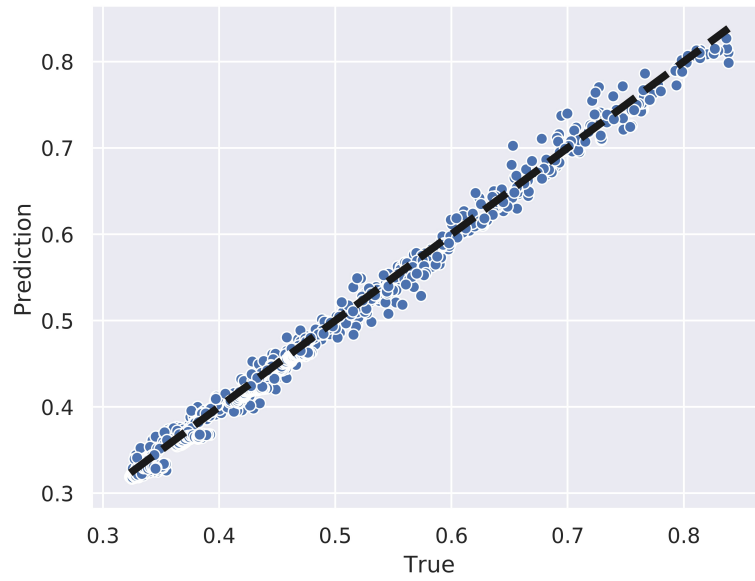
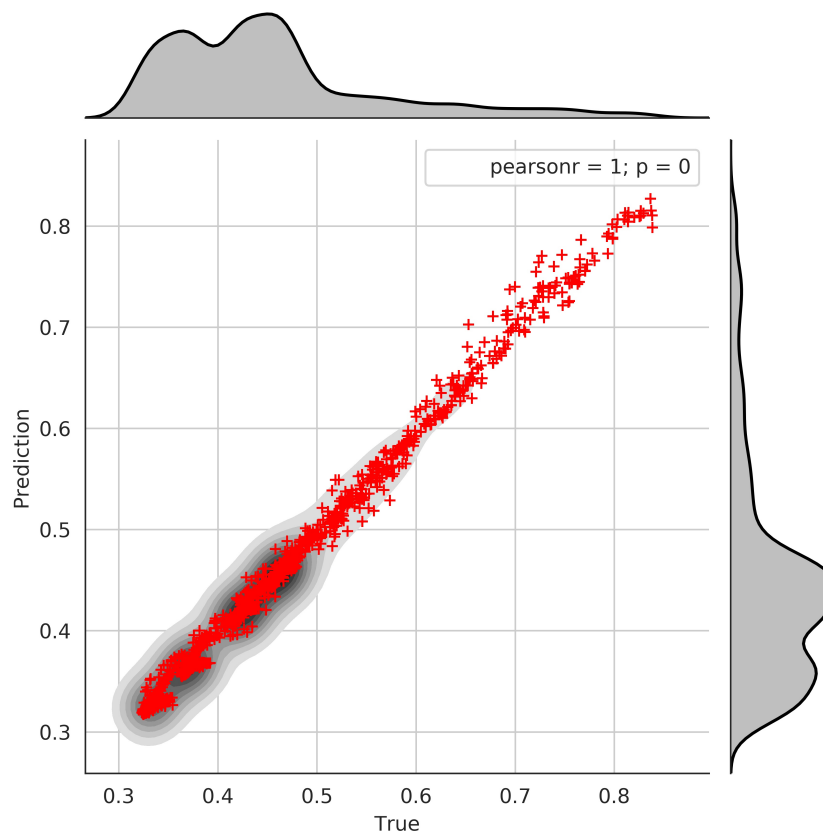


FIG. 17. Bland-Altman analysis plot of Q .

406 FOM-FSI for both cases are within 10%, while the relative errors δ of τ_0 and τ_s between
 407 the ROM-FSI and FOM-FSI for both of the cases are relatively larger. The difference could
 408 come from two sources: (a) in the GA optimization process, although the desired location
 409 and value of the optimized minimum cross-section area are preset to be equal to the target
 410 one (Eq. (7)), the actual optimized location of the minimum cross-section area may be
 411 shifted and the corresponding value may be changed especially for the divergent shape,
 412 which may affect the profile of the flow rate at the flow decreasing phase. To remedy this,
 413 further improvements on the UKE model may be considered, and (b) the ROM-FSI model



(a) Scatter plot



(b) Correlation plot

FIG. 18. Scatter and correlation plot of P_i .

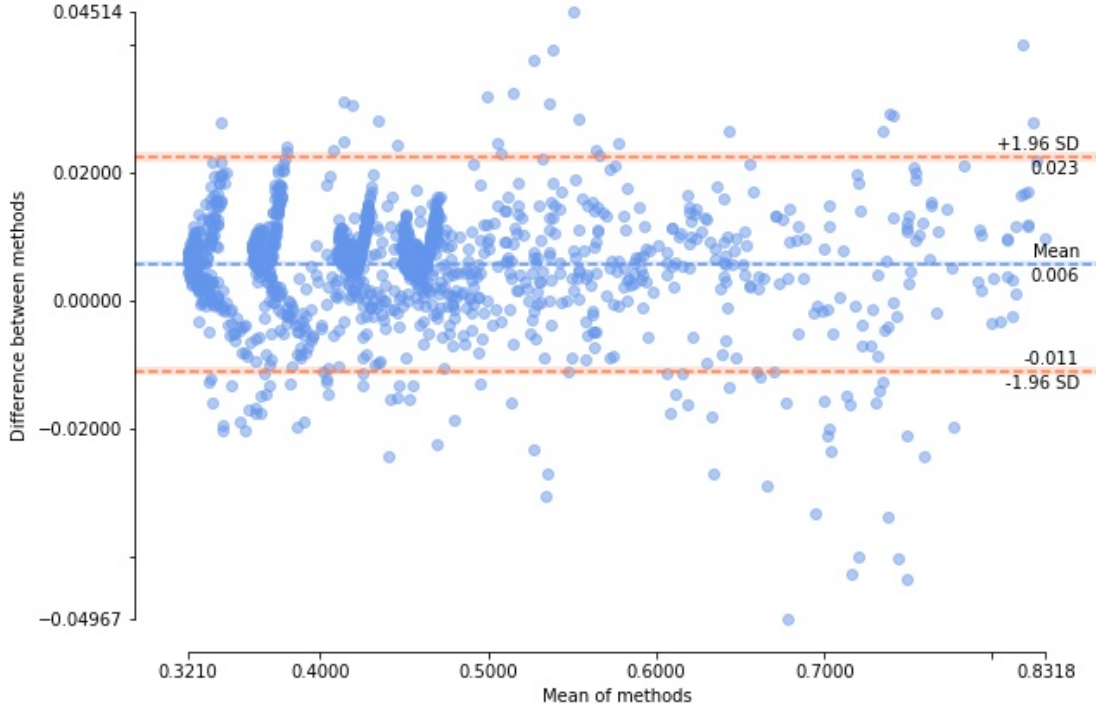


FIG. 19. Bland-Altman analysis plot of P_i .

414 is a quasi-steady model while the FOM-FSI is a fully unsteady model. The quasi-steady
 415 assumption might also contribute to the differences between the two models.

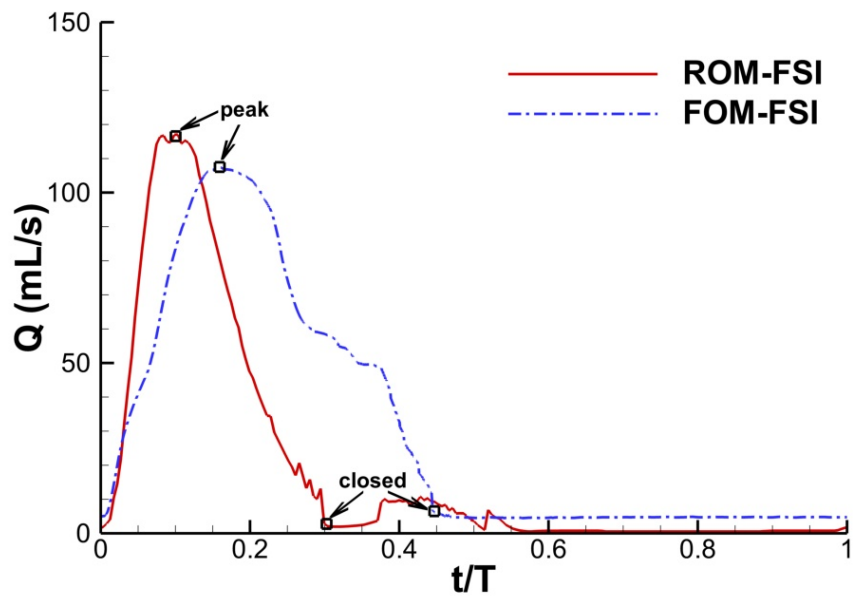
416 The comparison of the phase-averaged pressure distribution P_i for both cases are illus-
 417 trated in Figure 21. Note that T_0 is the duration of the glottal open phase probed from
 418 Figure 20 for each case. The overall agreement is good except at the flow decreasing phase.
 419 The glottal vibration patterns at the correspondent phases for both cases obtained by the
 420 ROM-FSI and FOM-FSI are compared in Figure 22. From the figure, we can see that the
 421 glottal vibration patterns obtained by the ROM-FSI agree well with those obtained by the

TABLE VI. Comparison of voice quality-related parameters.

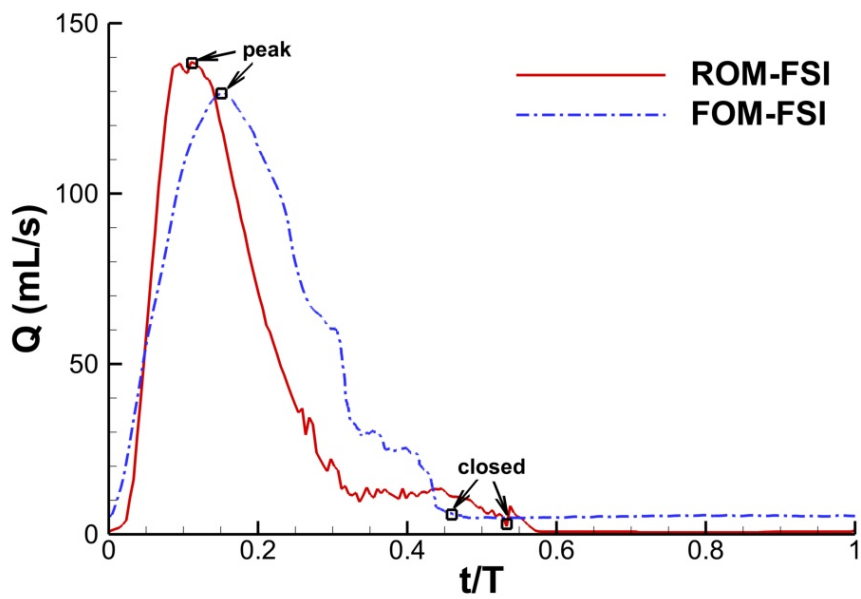
	ROM-FSI FOM-FSI		δ_1	ROM-FSI FOM-FSI		δ_2
	Case 1	Case 1		Case 2	Case 2	
	F_0 (Hz)	210.8		216.3	2.5%	
Q_{max} (mL/s)	117.0	107.3	9.0%	138.5	129.5	6.9%
Q_{mean} (mL/s)	54.8	56.6	3.2%	63.6	59.5	6.9%
τ_0	0.30	0.45	33.3%	0.53	0.46	15.2%
τ_s	0.49	0.55	10.9%	0.26	0.49	46.9%
ξ_m (cm)	0.060	0.055	9.1%	0.069	0.063	9.5%

F_0 is the fundamental frequency; Q_{max} and Q_{mean} are the peak and mean glottal flow rate of the open quotient, respectively; τ_0 is the open quotient, defined as $\tau_0 = T_0/T$, where T_0 is the duration of the glottal open phase and T is the cycle period; τ_s is the skewing quotient, defined as $\tau_s = T_p/T_n$ where T_p is the duration of the flow increasing phase and T_n is the duration of the flow decreasing phase (Xue *et al.*, 2014); ξ_m is the vibration amplitude; δ_1 and δ_2 are the absolute value of the relative error between the ROM-FSI and FOM-FSI results for Case 1 and Case 2, respectively.

422 FOM-FSI except at the flow decreasing phase. The discrepancies of the pressure distribution



(a) Case 1



(b) Case 2

FIG. 20. Comparison of the phase-averaged time history of the flow rate.

423 as well as the vibration patterns are consistent with those of the phase-averaged flow rate
424 shown in Figure 20.

425 The proper orthogonal decomposition (POD) analysis (Liang *et al.*, 2002) is employed
426 to extract the most energetic empirical eigen-modes from the snapshots of ROM-FSI and
427 FOM-FSI results for both cases. The three-dimensional and mid-coronal profile of the two
428 most energetic empirical eigen functions at two extreme phases for both cases are illustrated
429 in Figure 23. For both cases, these two modes contain around 98% of the total energy.
430 To precisely quantify the similarity between the two modes obtained by the ROM-FSI and
431 FOM-FSI, the dot-product between the corresponding normalized eigenmode (Xue *et al.*,
432 2011) for both cases is computed and plotted in Figure 24. The dot-product of any two
433 normalized modes is indicative of the similarity between the two modes with the value of
434 one corresponding to an exact match, and zero indicating orthogonality. From the figure, we
435 can observe that modes 1 and 2 obtained by the ROM-FSI are highly similar to the corre-
436 sponding modes obtained by the FOM-FSI for both cases which indicates a good prediction
437 performance of the present ROM for FSI simulation of the vocal fold vibration.

438 Furthermore, the average CPU time required for one vibration cycle of the ROM-FSI and
439 FOM-FSI simulation is compared. In order to obtain one vibration cycle, the average CPU
440 time required for the ROM-FSI simulation is 1.5 hours per CPU on a single CPU, while
441 that required for the FOM-FSI simulation is 20 hours per CPU on a parallel computer with
442 64 CPUs, which indicating the high efficiency of the present ROM for FSI simulation of the
443 glottal flow.

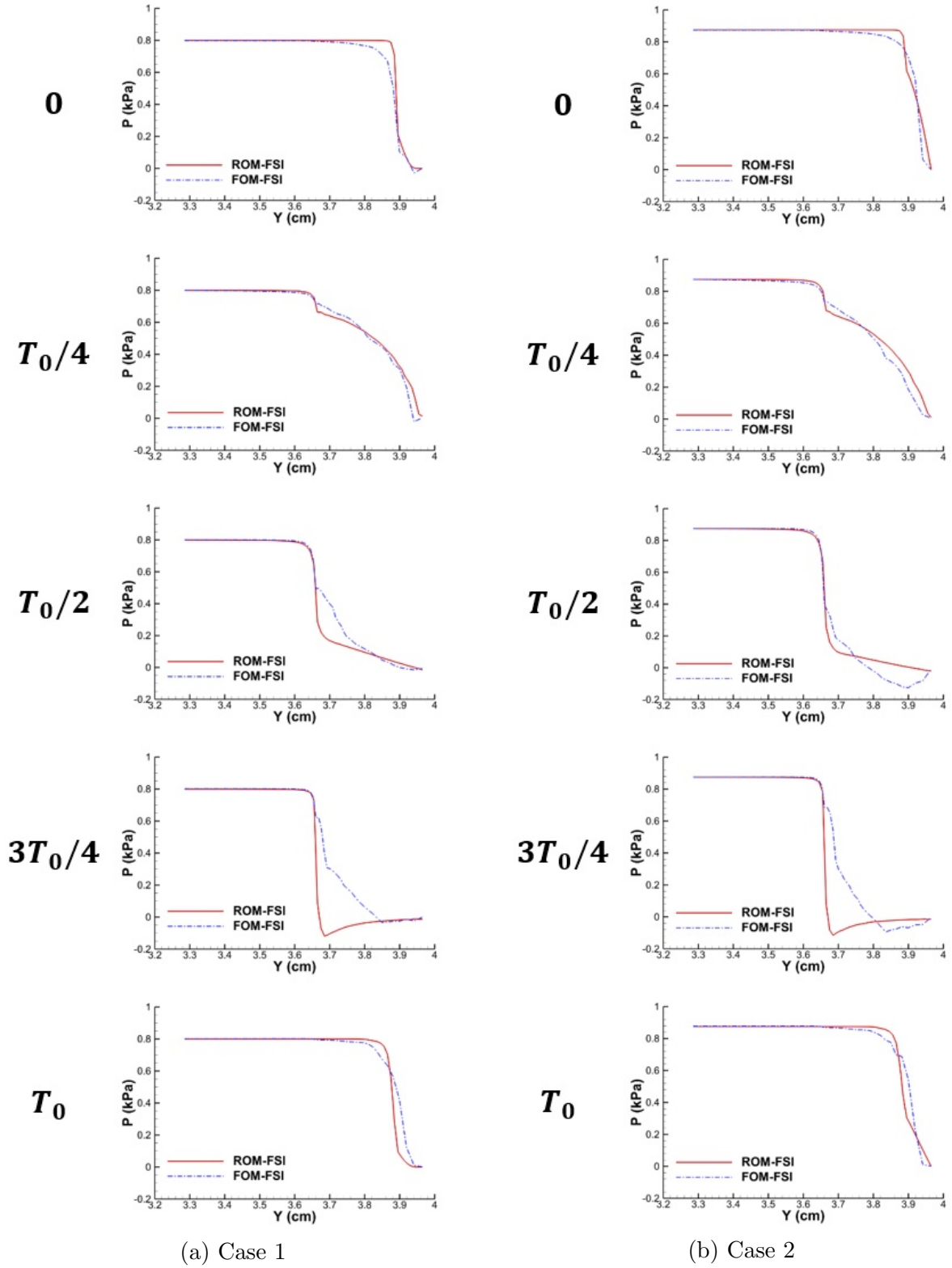


FIG. 21. Comparison of the phase-averaged pressure distribution.

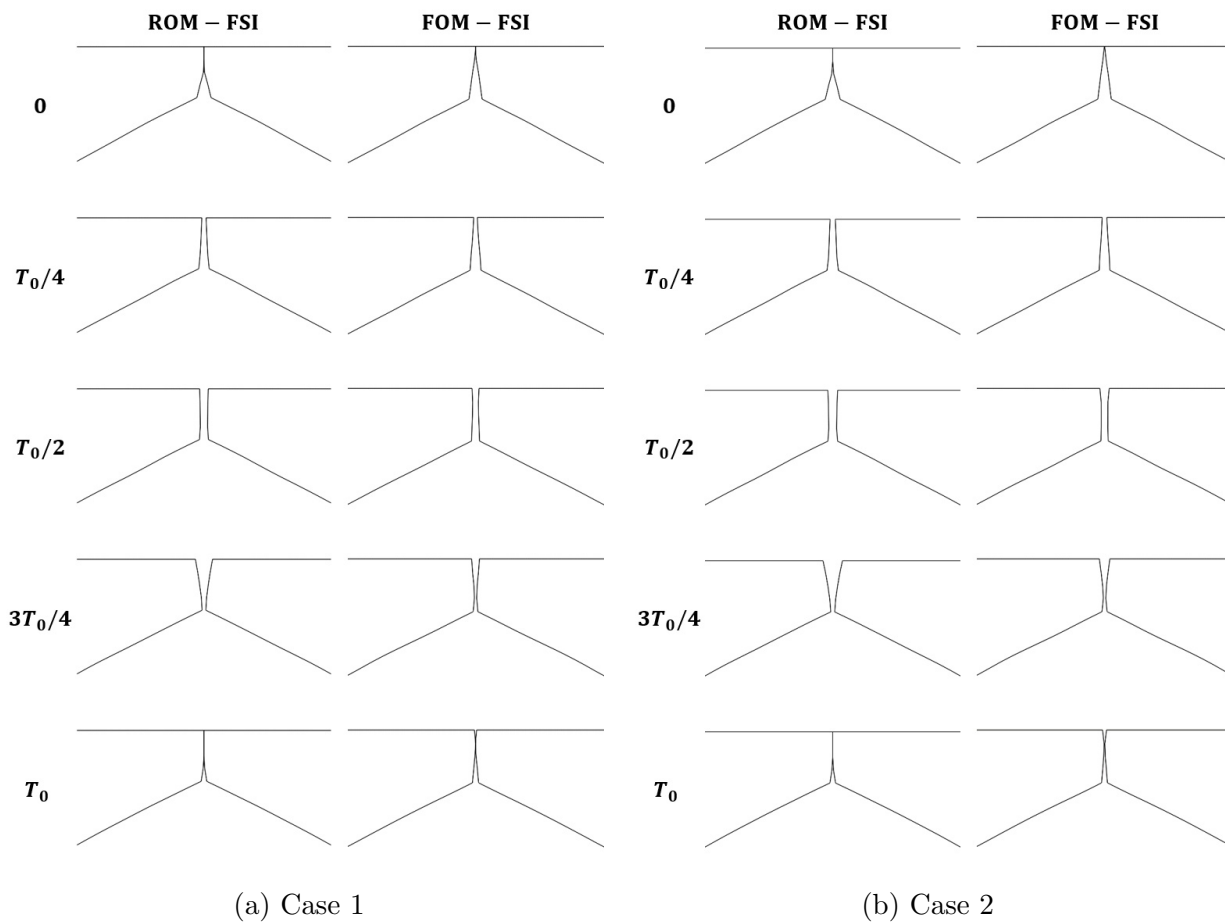


FIG. 22. Comparison of the vibration pattern at different phases in the coronal view.

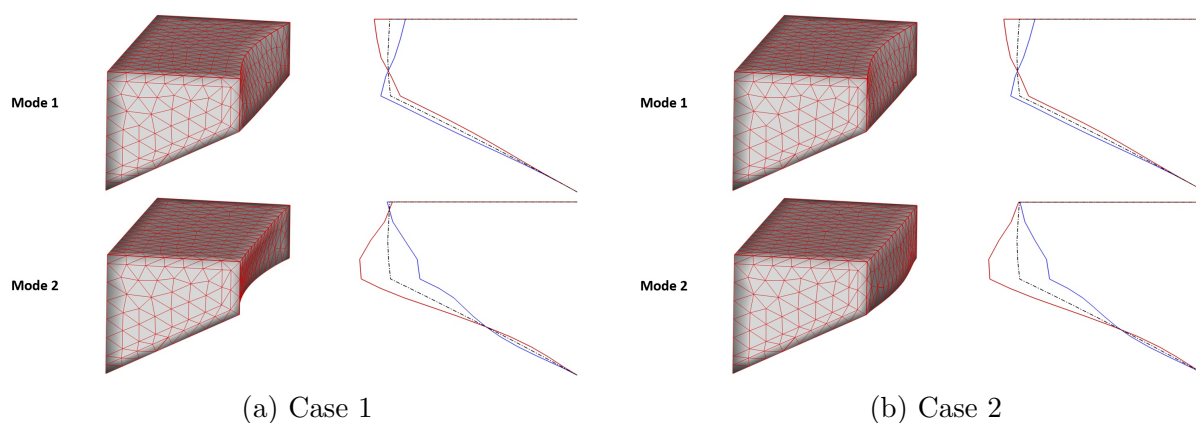


FIG. 23. Three-dimensional and mid-coronal profile of the most two energetic empirical eigen functions at two extreme phases (dash dot line: equilibrium position).

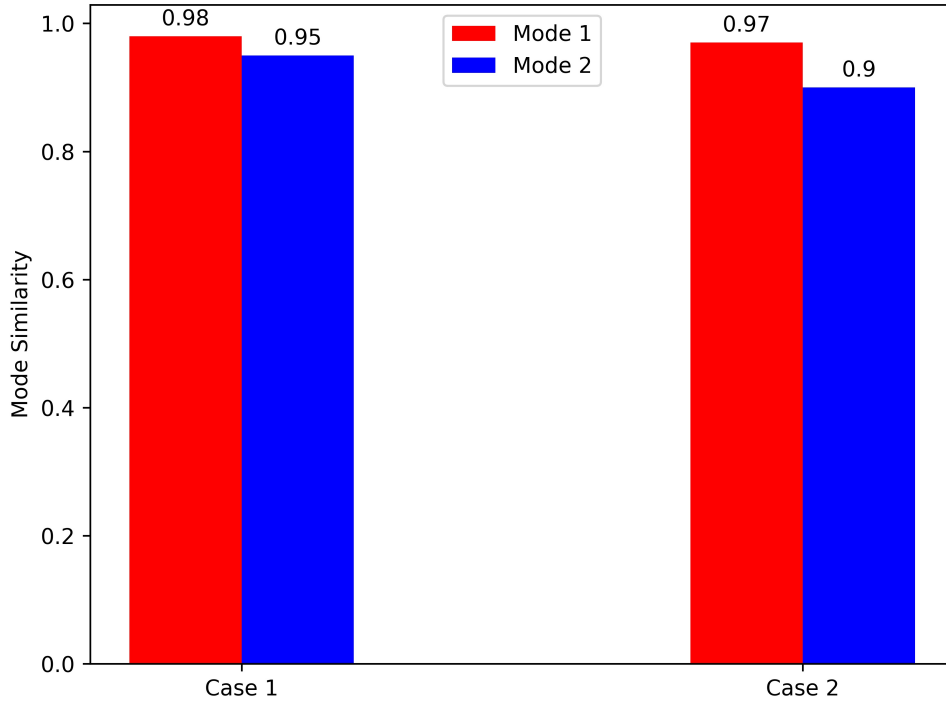


FIG. 24. Mode similarity.

444 **VI. CONCLUSION**

445 A deep-learning based generalized reduced-order model (ROM) that can provide fast and
 446 accurate prediction of the dynamics of the glottal flow during normal phonations is proposed
 447 in this paper.

448 The approach is based on the assumption that the vocal fold kinematics can be approxi-
 449 mated by a few vibration modes as described by the surface-wave approach. Therefore, the
 450 vibration of the vocal folds during normal phonations can be represented by a universal kine-
 451 matics equation (UKE) which is a linear combination of the dominant two modes. To verify
 452 that the UKE can be used as a generalized equation to represent any glottal shape during

453 normal phonation, A large number of glottal shapes are generated from Bernoulli-FEM FSI
454 simulation under various subglottal pressure and material properties and are fitted with a
455 UKE using the genetic algorithm (GA). Furthermore, the probability density function (PDF)
456 for each fitting parameter is obtained and used to build the generalized glottal shape library
457 by appropriately resampling the PDF of the parameters and substituting into the UKE. For
458 each shape in the library, the ground truth value of the flow rate and pressure distribution
459 are obtained from high-fidelity N-S solutions. A fully-connected deep neural network (DNN)
460 is used to build the empirical mapping between input parameters (parameters in the UKE
461 and subglottal pressure) and output parameters (flow rate and pressure distribution). K-fold
462 cross validation is performed to fine tune the architecture and hyperparameters and evaluate
463 the prediction performance of the DNN. The developed reduced order glottal flow model is
464 therefore composed of two parts: (a) glottal shape parameterization using the UKE and GA,
465 and (b) glottal flow rate and intraglottal pressure prediction using the trained DNN. The
466 present reduced-order flow solver is directly coupled with a finite-element method (FEM)
467 based solid dynamics solver for FSI simulation. The ROM-FSI results are compared with
468 the full-order model (FOM) quasi-static (QS) and FSI results. For the comparison with
469 the FOM-QS model, the ROM model shows an excellent agreement in terms of predicting
470 the flow rate and pressure distribution. The average error of the prediction for the flow
471 rate and pressure distribution are 7.87% and 1.68%, respectively. For the comparison with
472 the FOM-FSI model, the ROM model shows a good agreement on the frequency, peak and
473 mean flow rate and vocal fold vibration pattern with the relative errors less than 10%. The
474 ROM model shows a relatively larger error in predicting the opening quotient and skewness

475 quotient. The comparison of the details of the intraglottal pressure distribution between
476 the two models reflects that one of the reasons might be the inaccurate prediction of the
477 location of the minimum area when the glottis has a divergent shape. It should be noted
478 that the ROM-FSI model is a quasi-steady model while the FOM-FSI is a fully unsteady
479 model. The quasi-steady assumption might also contribute to the differences between the
480 two models. The overall good prediction performance of the present ROM in accuracy and
481 efficiency indicates a great promise for future clinical use. The developed ROM can be fur-
482 ther extended to predict the dynamics of the glottal flow during abnormal phonations with
483 relative ease.

484 **ACKNOWLEDGMENTS**

485 The project was supported by Grant Number 5R21DC016428 from the National Institute
486 on Deafness and Other Communication Disorders (NIDCD). Numerical simulations were
487 performed using resources of the Extreme Science and Engineering Discovery Environment
488 (XSEDE) (allocation Award Nos. TG-BIO150055 and TG-CTS180004).

489

490 Abadi, M., Agarwal, A., Barham, P., Brevdo, E., Chen, Z., Citro, C., Corrado, G. S.,
491 Davis, A., Dean, J., Devin, M., Ghemawat, S., Goodfellow, I., Harp, A., Irving, G., Isard,
492 M., Jia, Y., Jozefowicz, R., Kaiser, L., Kudlur, M., Levenberg, J., Mané, D., Monga,
493 R., Moore, S., Murray, D., Olah, C., Schuster, M., Shlens, J., Steiner, B., Sutskever, I.,
494 Talwar, K., Tucker, P., Vanhoucke, V., Vasudevan, V., Viégas, F., Vinyals, O., Warden,

495 P., Wattenberg, M., Wicke, M., Yu, Y., and Zheng, X. (2015). “TensorFlow: Large-scale
496 machine learning on heterogeneous systems” <https://www.tensorflow.org/>, software
497 available from tensorflow.org.

498 Alipour, F., Berry, D. A., and Titze, I. R. (2000). “A finite-element model of vocal-fold
499 vibration,” *The Journal of the Acoustical Society of America* **108**(6), 3003–3012.

500 Altman, D. G., and Bland, J. M. (1983). “Measurement in medicine: the analysis of method
501 comparison studies,” *Journal of the Royal Statistical Society: Series D (The Statistician)*
502 **32**(3), 307–317.

503 Berry, D. A. (2001). “Mechanisms of modal and nonmodal phonation,” *Journal of Phonetics*
504 **29**(4), 431–450.

505 Berry, D. A., Herzel, H., Titze, I. R., and Krischer, K. (1994). “Interpretation of biomechanical
506 simulations of normal and chaotic vocal fold oscillations with empirical eigenfunctions,”
507 *The Journal of the Acoustical Society of America* **95**(6), 3595–3604.

508 Chollet, F. *et al.* (2015). “Keras” .

509 Deverge, M., Pelorson, X., Vilain, C., Lagrée, P.-Y., Chentouf, F., Willems, J., and
510 Hirschberg, A. (2003). “Influence of collision on the flow through in-vitro rigid models
511 of the vocal folds,” *The Journal of the Acoustical Society of America* **114**(6), 3354–3362.

512 Döllinger, M., Berry, D. A., and Berke, G. S. (2005). “Medial surface dynamics of an in
513 vivo canine vocal fold during phonation,” *The Journal of the Acoustical Society of America*
514 **117**(5), 3174–3183.

515 Erath, B. D., Zañartu, M., Peterson, S. D., and Plesniak, M. W. (2011). “Nonlinear vocal
516 fold dynamics resulting from asymmetric fluid loading on a two-mass model of speech,”

517 Chaos: An Interdisciplinary Journal of Nonlinear Science **21**(3), 033113.

518 Forrest, S. (**1996**). “Genetic algorithms,” ACM Computing Surveys (CSUR) **28**(1), 77–80.

519 Freedman, D., Pisani, R., and Purves, R. (**2007**). International student edition *Statistics: Fourth International Student Edition* (W.W. Norton & Company), [https://books.](https://books.google.com/books?id=mviJQgAACAAJ)

520 [google.com/books?id=mviJQgAACAAJ](https://books.google.com/books?id=mviJQgAACAAJ).

521

522 Geng, B., Xue, Q., and Zheng, X. (**2016**). “The effect of vocal fold vertical stiffness variation

523 on voice production,” The Journal of the Acoustical Society of America **140**(4), 2856–2866.

524 Goldberg, D. (**2006**). *Genetic Algorithms* (Pearson Education), [https://books.google.](https://books.google.com/books?id=6gzS07Sv9hoC)

525 [com/books?id=6gzS07Sv9hoC](https://books.google.com/books?id=6gzS07Sv9hoC).

526 Goodfellow, I., Bengio, Y., and Courville, A. (**2016**). *Deep Learning* (MIT press).

527 Ishizaka, K., and Flanagan, J. L. (**1972**). “Synthesis of voiced sounds from a two-mass model

528 of the vocal cords,” Bell System Technical Journal **51**(6), 1233–1268.

529 Jiang, J. J., and Zhang, Y. (**2002**). “Chaotic vibration induced by turbulent noise in a

530 two-mass model of vocal folds,” The Journal of the Acoustical Society of America **112**(5),

531 2127–2133.

532 LeCun, Y., Bengio, Y., and Hinton, G. (**2015**). “Deep learning,” Nature **521**(7553), 436.

533 Liang, Y., Lee, H., Lim, S., Lin, W., Lee, K., and Wu, C. (**2002**). “Proper orthogonal de-

534 composition and its applications?Part I: Theory,” Journal of Sound and Vibration **252**(3),

535 527–544.

536 Luo, H., Mittal, R., Zheng, X., Bielamowicz, S. A., Walsh, R. J., and Hahn, J. K. (**2008**).

537 “An immersed-boundary method for flow–structure interaction in biological systems with

538 application to phonation,” Journal of Computational Physics **227**(22), 9303–9332.

539 Mitchell, M. (1998). *An Introduction to Genetic Algorithms* (MIT press).

540 Mittal, R., Zheng, X., Bhardwaj, R., Seo, J. H., Xue, Q., and Bielałowicz, S. (2011).
541 “Toward a simulation-based tool for the treatment of vocal fold paralysis,” *Frontiers in*
542 *Physiology* **2**, 19.

543 Pelorson, X., Hirschberg, A., Van Hassel, R., Wijnands, A., and Auregan, Y. (1994). “The-
544 oretical and experimental study of quasisteady-flow separation within the glottis during
545 phonation. application to a modified two-mass model,” *The Journal of the Acoustical*
546 *Society of America* **96**(6), 3416–3431.

547 Ruder, S. (2016). “An overview of gradient descent optimization algorithms,” arXiv preprint
548 arXiv:1609.04747 .

549 Ruty, N., Pelorson, X., Van Hirtum, A., Lopez-Arteaga, I., and Hirschberg, A. (2007). “An
550 in vitro setup to test the relevance and the accuracy of low-order vocal folds models,” *The*
551 *Journal of the Acoustical Society of America* **121**(1), 479–490.

552 Scherer, R. C., Titze, I. R., and Curtis, J. F. (1983). “Pressure-flow relationships in two
553 models of the larynx having rectangular glottal shapes,” *The Journal of the Acoustical*
554 *Society of America* **73**(2), 668–676.

555 Smith, S. L., and Titze, I. R. (2018). “Vocal fold contact patterns based on normal modes
556 of vibration,” *Journal of Biomechanics* **73**, 177–184.

557 Steinecke, I., and Herzel, H. (1995). “Bifurcations in an asymmetric vocal-fold model,” *The*
558 *Journal of the Acoustical Society of America* **97**(3), 1874–1884.

559 Story, B. H., and Titze, I. R. (1995). “Voice simulation with a body-cover model of the
560 vocal folds,” *The Journal of the Acoustical Society of America* **97**(2), 1249–1260.

561 Tao, C., and Jiang, J. J. (2008). “Chaotic component obscured by strong periodicity in
562 voice production system,” *Physical Review E* **77**(6), 061922.

563 Titze, I. R. (1988). “The physics of small-amplitude oscillation of the vocal folds,” *The*
564 *Journal of the Acoustical Society of America* **83**(4), 1536–1552.

565 Titze, I. R. (1994). *Principles of Voice Production* (Prentice Hall), [https://books.google.](https://books.google.com/books?id=m48JAQAAMAJ)
566 [com/books?id=m48JAQAAMAJ](https://books.google.com/books?id=m48JAQAAMAJ).

567 Van den Berg, J., Zantema, J., and Doornenbal Jr, P. (1957). “On the air resistance and the
568 bernoulli effect of the human larynx,” *The Journal of the Acoustical Society of America*
569 **29**(5), 626–631.

570 Wurzbacher, T., Schwarz, R., Döllinger, M., Hoppe, U., Eysholdt, U., and Lohscheller, J.
571 (2006). “Model-based classification of nonstationary vocal fold vibrations,” *The Journal*
572 *of the Acoustical Society of America* **120**(2), 1012–1027.

573 Xue, Q., Mittal, R., Zheng, X., and Bielamowicz, S. (2012). “Computational modeling
574 of phonatory dynamics in a tubular three-dimensional model of the human larynx,” *The*
575 *Journal of the Acoustical Society of America* **132**(3), 1602–1613.

576 Xue, Q., Zheng, X., Bielamowicz, S., and Mittal, R. (2011). “Sensitivity of vocal fold
577 vibratory modes to their three-layer structure: Implications for computational modeling
578 of phonation,” *The Journal of the Acoustical Society of America* **130**(2), 965–976.

579 Xue, Q., Zheng, X., Mittal, R., and Bielamowicz, S. (2014). “Subject-specific computational
580 modeling of human phonation,” *The Journal of the Acoustical Society of America* **135**(3),
581 1445–1456.

582 Zanartu, M., Mongeau, L., and Wodicka, G. R. (2007). “Influence of acoustic loading on
583 an effective single mass model of the vocal folds,” *The Journal of the Acoustical Society*
584 *of America* **121**(2), 1119–1129.

585 Zhang, L. T., and Yang, J. (2016). “Evaluation of aerodynamic characteristics of a coupled
586 fluid-structure system using generalized bernoulli’s principle: An application to vocal folds
587 vibration,” *Journal of coupled systems and multiscale dynamics* **4**(4), 241–250.

588 Zhang, Y., and Jiang, J. J. (2008). “Nonlinear dynamic mechanism of vocal tremor from
589 voice analysis and model simulations,” *Journal of Sound and Vibration* **316**(1-5), 248–262.

590 Zhang, Y., Zheng, X., and Xue, Q. (2020). “A deep neural network based glottal flow model
591 for predicting fluid-structure interactions during voice production,” *Applied Sciences* **10**(2),
592 705.

593 Zheng, X., Xue, Q., Mittal, R., and Beilamowicz, S. (2010). “A coupled sharp-interface
594 immersed boundary-finite-element method for flow-structure interaction with application
595 to human phonation,” *Journal of Biomechanical Engineering* **132**(11), 111003.